

Thesis

Ekaterina Avdeeva

University of Nebraska-Lincoln, USA

January 9, 2017

Abstract

This paper reviews

Contents

8	1	Introduction	2
9	1.1	Fundamental Particles and Interactions	3
10	1.2	Electroweak Interactions	5
11	1.3	Strong Interactions	8
12	1.4	Physics of Proton-Proton Collisions	9
13	1.5	Open Questions of the Standard Model	11
14	2	$W\gamma$ Production Theory and Former Experimental Results	12
15	2.1	Electroweak Theory of the Standard Model	13
16	2.2	Cross Section and Luminosity	18
17	2.3	Standard Model $W\gamma$ Production	20
18	2.4	Anomalous $W\gamma$ Production	23
19	2.5	Measurements in the Past	25
20	3	Experimental Setup	28
21	3.1	Large Hadron Collider	29
22	3.2	Compact Muon Solenoid	32
23	3.2.1	Introduction	32
24	3.2.2	Magnet	33
25	3.2.3	Tracking System	33
26	3.2.4	Electromagnetic Calorimeter	34
27	3.2.5	Hadron Calorimeter	35
28	3.2.6	Muon System	35
29	3.2.7	Triggering and Data Aquisition	36
30	3.2.8	Event Reconstruction	36
31	4	CMS Tracker Alignment	39
32	4.1	Algorithm	40
33	4.2	Selected Results	45
34	5	$W\gamma$ Cross Section Measurement	46

35 1 Introduction

36 Elementary particle physics describes fundamental particles and their interactions. Fundamental
37 particles are the smallest constituents of our Universe. When examined at smaller scales, the
38 substances around us consist of molecules, molecules consist of atoms. In an atom there is a
39 nucleus made of neutrons and protons and some number of electrons occupying orbits around
40 the nucleus. Protons and neutrons have a structure while an electron is not known to have any
41 internal structure, therefore, an electron is an example of a particle which is considered to be
42 fundamental.

43

44 Interactions of elementary particles are described by quantum field theories which incorporate
45 principles of the quantum mechanics and the special theory of relativity. The set of such theories,
46 including quantum electrodynamics (QED), quantum chromodynamics (QCD) and the theory
47 of weak interactions is called the Standard Model (SM). Current observations have proved the
48 SM to be an accurate description of elementary particle interactions.

49

50 However, there are several experimental observations that are not described by the SM such
51 as effects of gravity, dark matter, dark energy, matter/antimatter asymmetry and others. There-
52 fore, the SM is not the complete theory of particle interactions. There are several SM extensions
53 offered by theorists as well as radically new theories waiting for experimental confirmation or
54 exclusion.

55

56 Some SM extensions and new theories predict the existence of heavy particles with masses
57 lying beyond experimentally reachable energies. The search of these particles is a priority in
58 particle physics. One source of highly energetic elementary particles is cosmic rays. The most
59 energetic particles ever observed came from this source. However, cosmic rays are totally uncon-
60 trollable and such highly energetic particles are rare. If we want to produce a large number of
61 particles in a given energy range, we need to use a particle accelerator. A large amount of data
62 allows experimentalists to perform a statistical analysis and increase the probability of finding a
63 new particle if it exists.

64

65 Symmetric colliding beams is the most effective way to produce as heavy particles as possible
66 given the energies of the colliding particles. Compared to experiments colliding a single beam at
67 a fixed target, in the case of a symmetric collision the total momentum of two colliding particles
68 is zero and, therefore, much larger fraction of energy can transfer to a mass of a new particle.
69 The Large Hadron Collider (LHC) is one such collider with the highest energy in the world. It
70 can produce the most massive particles to probe physics beyond the SM (BSM).

71

72 The Compact Muon Solenoid (CMS) is one of two general-purpose detectors at the LHC. It
73 is placed at one of four collision points. CMS has a broad physics program including searches for
74 the BSM physics as well as the precision measurements of the parameters of the SM itself. The
75 measurement of this dissertation is a SM measurement with CMS data collected in 2012 in pp
76 collisions of LHC with beam energies of 4 TeV. The result can be compared to the SM prediction.
77 Certain BSM theories predict a deviation of the result of this measurement from its SM value,
78 therefore, with this measurement, in addition to testing the SM, we also search for a new physics.

79

80 The rest of this chapter gives general introductory information about the SM while Ch. 2
81 concentrates on the theory of the SM and BSM $W\gamma$ production and also discusses previous
82 measurements of this process. Chapter 3 describes LHC and CMS in more details. Chapter 4
83 explains one specific detail of the CMS operation that is the spacial alignment of the tracking
84 detector of charged particles. Finally, Ch. 5 describes the details of the measurement of this
85 dissertation and reports the results.

86

87 1.1 Fundamental Particles and Interactions

88 The SM describes interactions of elementary particles. There are four fundamental interactions:
89 electromagnetic, strong, weak and gravitational. The gravity is not included into the SM but its
90 effect on particles is negligible compared to the other forces which makes it possible to develop a
91 theory of the particle physics and conduct experiments even without having the gravity included
92 into the model.

93
94 All fundamental elementary particles in the SM can be split into three categories by their
95 spins. There are fermions which possess spin $s=1/2$, there are gauge bosons which are vector
96 particles ($s=1$) and there is the Higgs boson which is a scalar particle ($s=0$).

97
98 The fermions are arranged into three generations, each generation consists of a quark with
99 charge $Q=+2/3$ (up, charm, and top quarks), a quark with $Q=-1/3$ (down, strange, and bottom
100 quarks), a charged lepton with $Q=-1$ (electron, muon, and tau-lepton) and a neutrino (electron,
101 muon, and tau neutrinos) which is electrically neutral. Each quark can carry any of three colors:
102 red, blue, or green. Additionally, each fermion has its antiparticle. Therefore, the total number
103 of fundamental fermions is $(6(\text{leptons}) + 6(\text{quarks}) \cdot 3(\text{colors})) \cdot 2(\text{to include antiparticles}) = 48$.

104
105 Corresponding particles in different generations have the same charges, spins and interaction
106 properties but masses of particles increase with a generation. These mass differences lead
107 to different decay properties because a particle A can decay to particles B and C only if their
108 masses relate as $m_A > m_B + m_C$. Thus, an electron is a stable particle, a muon decays as
109 $\mu^- \rightarrow e^- + \bar{\nu}_e + \nu_\mu$, a tau-lepton, as the heaviest charged lepton, has the largest number of decay
110 channels amongst the charged leptons: $\tau^- \rightarrow \mu^- + \bar{\nu}_\mu + \nu_\tau$, $\tau^- \rightarrow e^- + \bar{\nu}_e + \nu_\tau$, $\tau^- \rightarrow \nu_\tau + \text{quarks}$.

111
112 In addition to fermions, the SM includes gauge bosons which are interaction mediators. They
113 are called mediators because fermions interact with each other by exchanging them. For example,
114 two charged fermions can interact with each other by exchanging a photon. Such interaction is
115 called electromagnetic interaction and a photon is a mediator for the electromagnetic interaction.
116 Similarly, a gluon is a mediator for strong interactions, and W^\pm and Z^0 bosons are mediators
117 for weak interactions. W^\pm and Z^0 bosons are massive while a photon and a gluon are massless
118 particles.

119
120 The last SM particle is the Higgs boson. The Higgs boson is a scalar neutral particle which
121 is playing a critical role in the electroweak symmetry breaking. The Higgs mechanism explains
122 how W and Z bosons become massive particles.

123
124 All the particles are summarized in Fig. 1. These and only these fundamental particles and
125 their antiparticles have been discovered by now. However, there are many composite particles
126 which are called hadrons. Hadrons can consist of three quarks (baryons), quark and antiquark
127 (meson), or three antiquarks (antibaryons). Hadrons always possess an integer charge.

128
129 Most of the particles are short-lived and decay within microseconds. The only stable particles
130 are protons and antiprotons, electrons and positrons, neutrinos and antineutrinos, photons,
131 and, in some sense, gluons. However, if a particle cannot decay, it does not mean that it would
132 live forever. There are many different kinds of reactions in which particles can disappear. An-
133 tiprotons and positrons would immediately annihilate with protons and electrons, photons can
134 be absorbed by charged particles, electrons and protons can scatter to produce neutrons and
135 neutrinos and many other reactions are possible.

136
137 In this dissertation, the study of $pp \rightarrow W\gamma + X \rightarrow l\nu\gamma$ process where $l = e, \mu$ is presented. The
138 $W\gamma$ production with leptonic W decays proceeds through one of the following three processes:
139 the initial state radiation where a photon is emitted from one of the incoming partons, the final
140 state radiation where a photon is radiated off the charged lepton from the W boson decay, and,
141 finally, the triple gauge coupling (TGC) where a photon is emitted from the W boson. Many

142 BSM theories predict an enhancement of the TGC production over the SM value and, therefore,
 143 the experimental search for such an enhancement is a good test for such theories.

144
 145 Therefore, the focus of this study is an interaction between a photon and a W boson however
 146 many other SM particles are relevant too. Thus, a charged lepton and a neutrino appear as the
 147 final state particles, a quark and an antiquark appear as initial state particles and all fundamental
 148 particles except the Higgs boson participate in various background processes. Subsequent
 149 chapters describe these particle interactions in more details.
 150

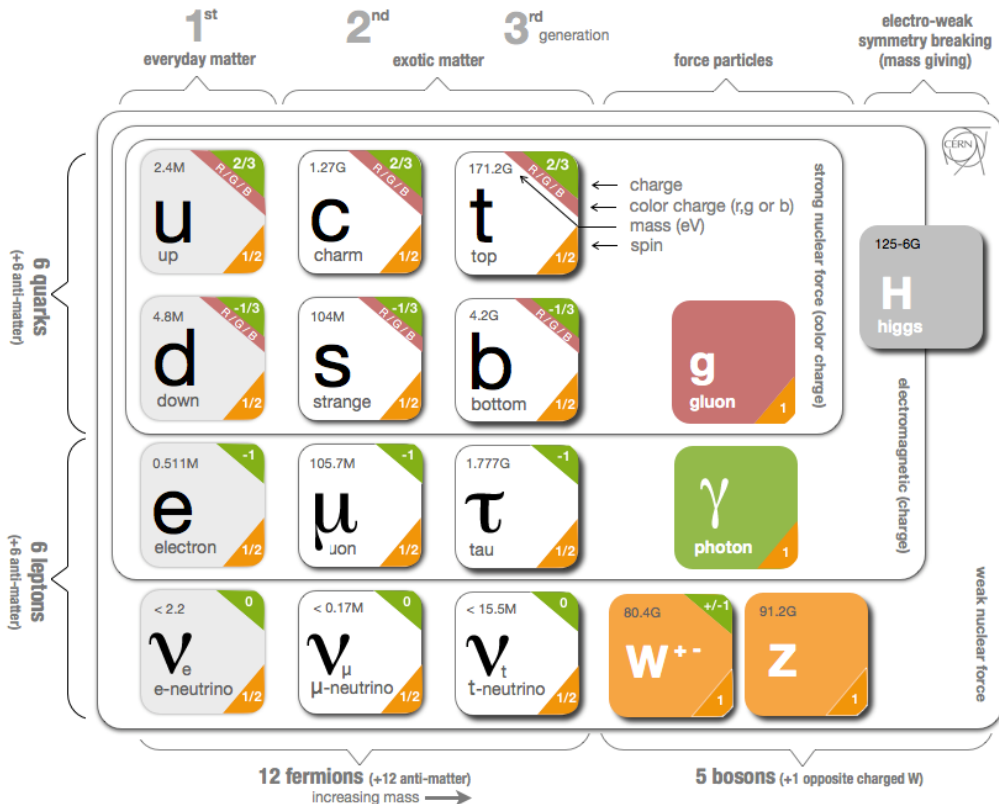


Figure 1: Standard Model Particles and Interactions. Source of the figure: [2].

151 **1.2 Electroweak Interactions**

152 All electrically charged particles participate in electromagnetic interactions. The theory of elec-
 153 tromagnetic interactions is called quantum electrodynamics (QED). All electromagnetic inter-
 154 actions are mediated by a photon, a spin-one electrically neutral massless particle, and can be
 155 reduced to one elementary process (Fig. 2, left). This process represents a charged fermion
 156 radiating or absorbing a photon. Such elementary process itself is forbidden by the energy con-
 157 servation law but this element is a base of an actual process. For example, the Bhabha scattering,
 158 $e^+e^- \rightarrow e^+e^-$, occurs through e^+e^- annihilation with further production of a new e^+e^- pair
 159 (Fig. 2, middle) or through exchange of a photon between the positron and the electron (Fig. 2,
 160 right). Both cases involve nothing except the electromagnetic elementary process (Fig. 2, left).
 161 Such graphical representations of the particle physics processes are called Feynman diagrams.

162

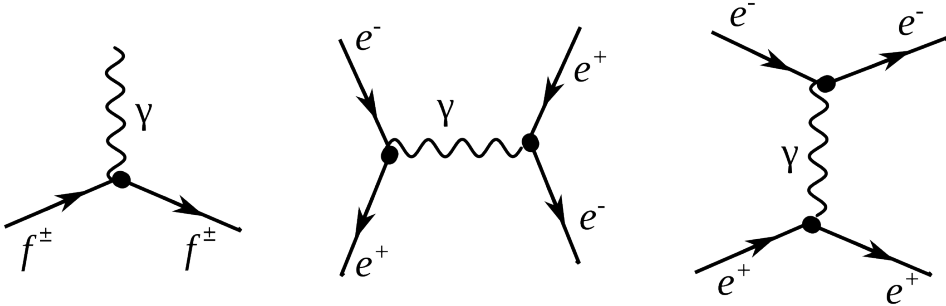


Figure 2: Electromagnetic interactions. Left: a photon radiation off a charged fermion, middle and right: Bhabha scattering.

163 As for the weak interactions, there are two kinds of them: neutral (mediated by a Z boson)
 164 and charged (mediated by a W^\pm boson). Elementary processes with W and Z bosons are shown
 165 in Fig. 3. Because the electric charge must be conserved at any vertex, a particle radiating or
 166 absorbing a W boson converts to a different particle. Thus, a charged lepton converts to a neu-
 167 trino (or vice versa) as shown in Fig. 3, top middle. Each lepton carries a lepton flavor number
 168 (Tab. 1). Lepton flavor is conserved in any interaction, thus an electron radiating a W boson
 169 always converts to an electron neutrino, a muon converts to a muon neutrino etc.

170

Table 1: Lepton Flavor Number

particles	L_e	L_μ	L_τ
e^-, ν_e	+1	0	0
$e^+, \bar{\nu}_e$	-1	0	0
μ^-, ν_μ	0	+1	0
$\mu^+, \bar{\nu}_\mu$	0	-1	0
τ^-, ν_τ	0	0	+1
$\tau^+, \bar{\nu}_\tau$	0	0	-1

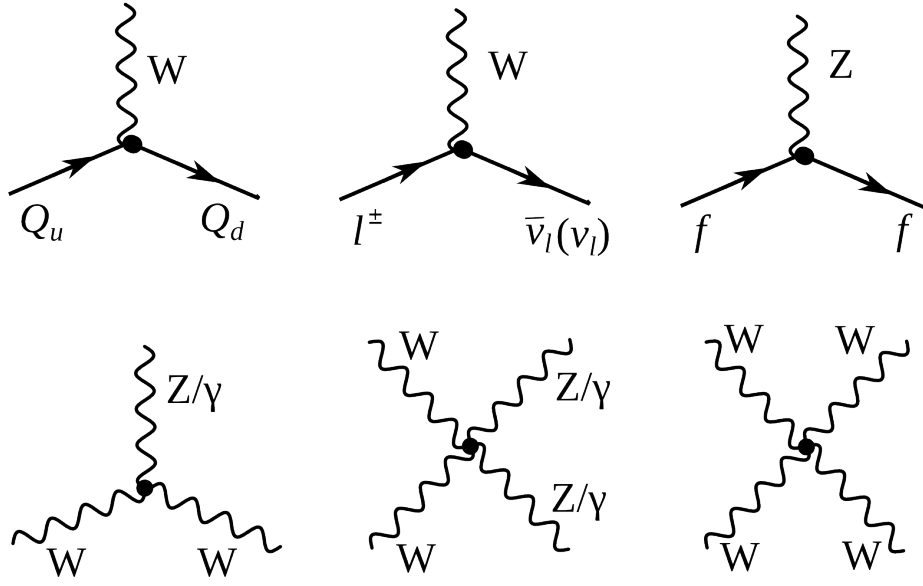


Figure 3: Weak elementary processes and gauge couplings. Top left: a quark with charge $Q=+2/3$ enters, emits a W boson, and a quark with charge $Q=-1/3$ escapes. Top middle: a charged lepton enters, emits a W boson, and a neutrino or antineutrino escapes conserving a lepton flavor number. Top right: a fermion enters, emits a Z boson and escapes. Bottom left: TGC couplings $WW\gamma$ and WWZ . Bottom middle: QGC couplings $WW\gamma\gamma$, $WWZ\gamma$ and $WWZZ$. Bottom right: QGC coupling $WWWW$.

From top left diagram in Fig. 3 we see that if a quark with $Q=+2/3$ enters, then a quark with $Q=-1/3$ escapes and, therefore, the flavor of the quark is changed. The charged weak interaction is the only interaction which changes a quark flavor. The probability of each of three quarks with $Q=-1/3$ to be born is determined by the Cabibbo-Kobayashi-Maskawa matrix which relates mass eigenstates d , c and b to weak eigenstates d' , c' and b' (Eq. 1). Absolute values of the matrix elements are all known (Eq. 2) and are the highest for the quark of the same generation as an initial state quark. In the particular case shown in the top left diagram in Fig. 3, u is the initial state quark and d has the highest probability to be produced after an interaction with a W boson but s and b can also be produced if there is enough energy.

180

$$\begin{pmatrix} d' \\ s' \\ b' \end{pmatrix} = \begin{pmatrix} V_{ud} & V_{us} & V_{ub} \\ V_{cd} & V_{cs} & V_{cb} \\ V_{td} & V_{ts} & V_{tb} \end{pmatrix} \begin{pmatrix} d \\ s \\ b \end{pmatrix} \quad (1)$$

$$\begin{pmatrix} |V_{ud}| & |V_{us}| & |V_{ub}| \\ |V_{cd}| & |V_{cs}| & |V_{cb}| \\ |V_{td}| & |V_{ts}| & |V_{tb}| \end{pmatrix} = \begin{pmatrix} 0.97 & 0.23 & 0.00 \\ 0.23 & 0.97 & 0.04 \\ 0.01 & 0.04 & 1.00 \end{pmatrix} \quad (2)$$

An elementary process of a neutral weak interaction is an emission a Z boson off a fermion line (right top diagram in Fig. 3). Diagrams with a Z boson are very similar to ones with a photon except a photon can only be radiated off a charged particle but a Z boson can also be radiated off a neutrino or antineutrino.

185

186 The bottom diagrams in Fig. 3 are gauge bosons coupling diagrams including self-coupling
 187 of a W boson, its interaction with a Z boson and its electromagnetic radiation of a photon.
 188 Charge-conserving TGC and quartic gauge couplings (QGC) containing two or four W bosons
 189 are all possible in the SM: WWZ , $WW\gamma$, $WWZZ$, $WWZ\gamma$, $WW\gamma\gamma$, and $WWWW$.
 190

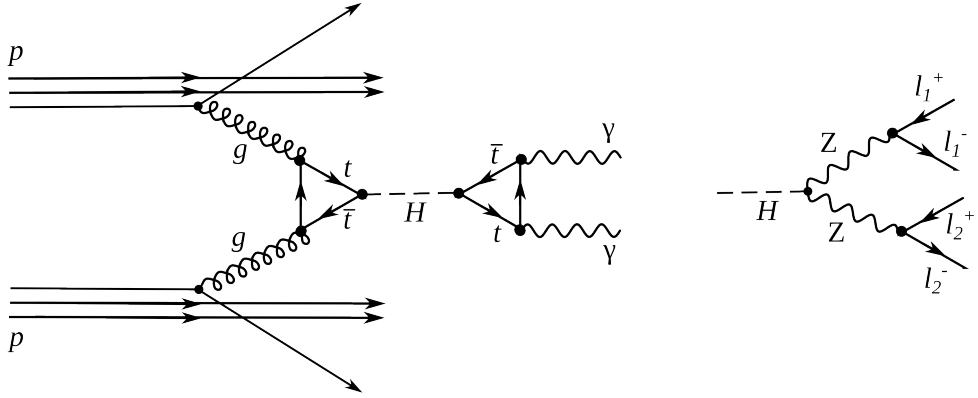


Figure 4: The Higgs boson production and decay. Left: $H \rightarrow \gamma\gamma$, right: $H \rightarrow ZZ \rightarrow 4l$.

191 Electromagnetic and weak interactions are unified by the electroweak Glashow-Weinberg-
 192 Salam (GWS) theory which is based on $SU(2) \times U(1)$ symmetry. $SU(2)$ is the symmetry of
 193 weak isospin which generates three bosons: W^1 , W^2 and W^3 . $U(1)$ is the symmetry of the weak
 194 hypercharge and generate one neutral boson B . W^1 and W^2 are mixed to create W^+ and W^-
 195 mediators while W^3 and B are mixed to create a Z boson and a photon. Therefore, the GWS
 196 theory considers electromagnetic and weak forces as different manifestations of the electroweak
 197 force. The electroweak theory is discussed in greater details in Ch. 2.

198 However, weak interactions are mediated by heavy bosons ($M_W = 80$ GeV, $M_Z = 91$ GeV)
 199 while electromagnetic interactions are mediated by a massless photon, thus, the electroweak
 200 symmetry is broken. To explain this phenomenon, the Higgs mechanism was introduced. The
 201 mechanism predicted an existence of an additional boson: the Higgs boson. The Higgs boson
 202 was a missing piece of the SM for many years and was finally discovered in 2012 at LHC by
 203 ATLAS and CMS collaborations through the processes shown in Fig. 4 [3], [4].
 204

205 The measurement in this dissertation is an electroweak measurement because the process
 206 involves a W boson. It includes an interaction of a W boson with leptons and quarks as well as
 207 the TGC $WW\gamma$. Thus, the measurement is a good test of the SM electroweak theory.
 208

209

210 1.3 Strong Interactions

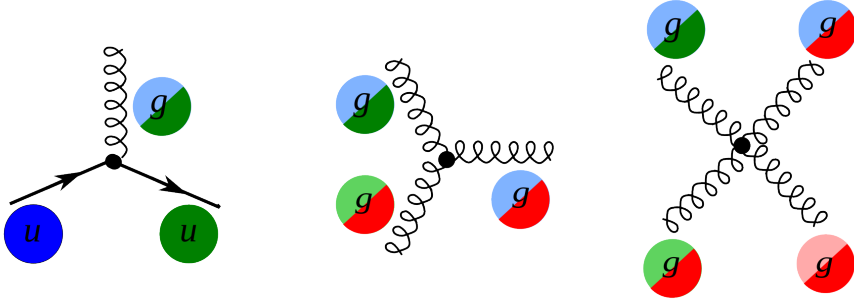


Figure 5: Elementary processes of strong interactions

211 The third fundamental force after the electromagnetic and weak ones is the strong force. The
212 strong force is responsible for gluing protons and neutrons together in the nuclei as well as for
213 forming protons and neutrons themselves. The strong interactions occur by exchanging gluons
214 which are spin-one massless electrically neutral particles.

215

216 The elementary strong processes are shown in Fig. 5. There are three elementary processes:
217 qqg , ggg and $gggg$, all are involving particles with color charges. Thus, gluons couple to quarks
218 and self-couple. Color charges must be conserved at each elementary process of the strong inter-
219 action. Each quark possesses one of three colors at a time, and there are eight types of gluons
220 to cover all possible color exchanges.

221

222 The coupling constant of the strong interaction depends on a distance between interacting
223 particles: it becomes larger as the distance becomes larger and smaller as the distance becomes
224 smaller. As the distance approaches zero, the coupling constant approaches zero too, and, thus,
225 in the asymptotic limit two quarks located at the same place do not interact. This property is
226 called asymptotic freedom.

227

228 On the other hand, when the distance between quarks becomes larger, the coupling constant
229 also becomes larger. This property confines quarks to always stay in the color neutral combi-
230 nations (hadrons), it forbids the existence of free quarks. A combination becomes color neutral
231 when there is the same amount of color and anticolor or if there is the same amount of each of
232 the three colors. Thus, mesons are comprised of a quark and an antiquark with the opposite
233 color charges, and baryons are comprised of three quarks: red, green and blue one. Examples of
234 baryons include such well-known particles as a proton and a neutron.

235

236 The asymptotic freedom and the confinement are properties that are specific for strong inter-
237 actions. The theory of strong interactions is called the quantum chromodynamics (QCD)
238 which is a quantum field theory invariant under $SU(3)$ color transformations. When the cou-
239 pling constant is much less than one $\alpha_s \ll 1$, the perturbative approach can be used to compute
240 observables.

241

242 The $W\gamma$ process being measured in this dissertation is not intended to test QCD, but a good
243 understanding of QCD is essential for performing this measurement because the QCD correc-
244 tions to the Feynman diagrams of the process are large and have to be taken into account when
245 producing simulation. In addition, QCD describes the dynamics of quarks and gluons within
246 colliding protons and predicts probabilities of one or another quark-antiquark pair to interact.
247 Physics of proton-proton collisions is discussed in the Ch. 1.4.

248

249 1.4 Physics of Proton-Proton Collisions

250 Consider a pp collision at LHC. The proton energies are so high that each proton behaves as a
 251 complex structure. A proton is a baryon, it consists of three quarks: uud . These three quarks
 252 are called valence quarks. They interact with each other by exchanging gluons which produce
 253 virtual $q\bar{q}$ pairs (Fig. 6). Such quarks are called sea quarks.

254 Any parton from one proton can interact with any parton from another proton. Probabilities
 255 $f_i(x, Q^2)$ of any particular constituent i to interact are described partially by QCD and parti-
 256 cally by experimental measurements and depend on the momentum transfer Q and the momen-
 257 tum fraction of a specific parton x . These probabilities are called parton distribution func-
 258 tions (PDFs).

260

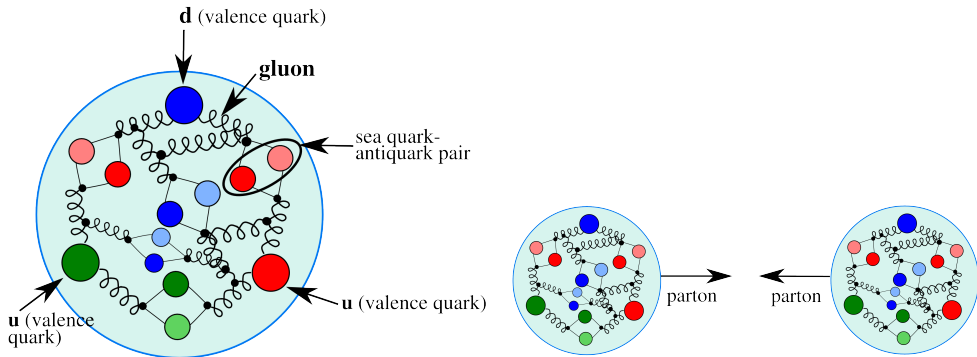


Figure 6: The proton structure (left) and the proton-proton collision (right).

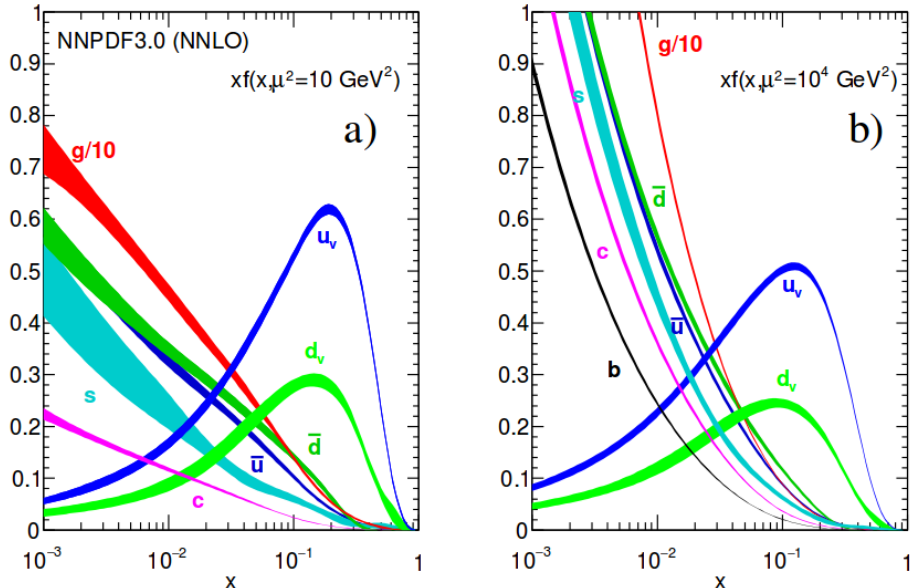


Figure 7: Parton distribution functions [5].

261 For large Q^2 and x gluon-gluon interactions have the largest probabilities to occur (Fig. 7).

262 However, gluons do not couple directly to a W boson, thus, in the $W\gamma$ measurement we are
263 mostly interested in quark-antiquark pairs which would have a total charge corresponding to the
264 charge of a W boson (± 1). Since we have u and d as valence quarks and we know that the
265 probability to couple to the same generation quark in charged weak interactions is the highest,
266 most of the W bosons are created by $u\bar{d}$ and $d\bar{u}$ pairs however other $q\bar{q}'$ combinations with the
267 total charges of ± 1 are also possible. As we look for events containing $W\gamma$ we also have other
268 events mimicking our process. Such background events can be produced by any pair of partons.

269

270 1.5 Open Questions of the Standard Model

271 While the SM is an accurate description of all particle physics experimental results, there are
272 certain phenomena which are not included into the SM. In this subsection we discuss some of
273 them.

274 The gravitational interactions do not fit into the SM. It is the open question whether the
275 quantum theory of gravity is possible and whether there is a mediator of the gravitational in-
276 teractions. Also, it is not known why the gravitational force is so much weaker than the other
277 forces. One possible explanation comes from a theory which predicts extra spatial dimensions
278 beyond the three we experience (e.g. the string theory). In this case, it is possible that the
279 gravitational force is shared with other dimensions and only a fraction is available in our three
280 dimensions.
281

282 Another mystery of the universe is its composition: it is known from the studies of the grav-
283 itational effects that our universe consists of dark energy by 68%, of dark matter by 27% and of
284 baryon matter only by 5% [6]. The dark energy resists the gravitational attraction and acceler-
285 ates the expansion of the universe, and is not detectable by any effects except gravitational. The
286 understanding of dark energy is a question of general relativity rather than particle physics. The
287 dark matter, however, likely consists of particles and therefore is a subject of particle physics.
288 It does not radiate and that is why it cannot be detected by telescopes. The nature of the dark
289 matter is not known but its constituents must be very stable to remain since the Big Bang. The
290 theory of the supersymmetry which is unifying fundamental particles and mediators predicts
291 many of new heavy particles and the lightest supersymmetric particle, the neutralino, is a good
292 candidate for dark matter.
293

294 One more open question is the reason for the matter/antimatter asymmetry. Matter and
295 antimatter should have been created in the same amount at the moment of the Big Bang. Most
296 of it has annihilated but because of asymmetry, there was more matter than antimatter which
297 led to the state of the Universe we observe now. There is a phenomenon of the CP-violation
298 in weak interactions observed and described which predicts the asymmetry at a certain level.
299 However, the effect of the CP-violation is not large enough to account for the observed amount
300 of the matter and, therefore, the total matter/antimatter asymmetry remains unexplained.
301

302 The measurement of the photon transverse momentum spectrum (P_T^γ) of the $W\gamma$ process has
303 a goal to both test the SM and search for the BSM physics. The low P_T^γ region is not expected
304 to be affected by any new physics and must agree well with the SM predictions while the high
305 P_T^γ region may indicate an existence of new physics if there is an enhancement over the SM
306 predictions. The excess would be indirect evidence of the BSM particles like supersymmetric
307 particles or additional gauge bosons which could be part of the explanation of the dark matter
308 presence or difference in magnitudes of different interactions. More theoretical details about the
309 SM description of $W\gamma$ process as well as possible BSM physics are given in Ch. 2.
310

312 2 $W\gamma$ Production Theory and Former Experimental Re- 313 sults

314 Chapter 2 provides deeper theoretical background for the measurement of this dissertation and
315 discusses former experimental results. The derivation of the electroweak Lagrangian is described
316 in Ch. 2.1, including the appearance of TGC and QGC terms. Then concepts of the cross section
317 and the luminosity are discussed in Ch. 2.2. More specific details regarding the SM cross section
318 of $W\gamma$ are summarized in Ch. 2.3. Possible causes and potential effects of aTGC are explained in
319 Ch. 2.4. Finally, Ch. 2.5 lists former physics experiments which probed the same aTGC vertex
320 which is probed in the measurement of this dissertation including measurements of exactly the
321 same process at lower LHC beam energy.

322

323 2.1 Electroweak Theory of the Standard Model

324 To develop a quantum field theory, we start with the Lagrangian of free fermions. In order
325 to describe a system with a conservation of a physical quantity, the Lagrangian is required to
326 satisfy a local invariance with respect to a certain transformation. For instance, a conservation
327 of an electric charge requires a local invariance under $U(1)$ transformation for the QED La-
328 grangian [7]. The requirement of the local invariance introduces an interaction of a new vector
329 field (or several fields) with our free fermions. The new vector field is a mediator of an inter-
330 action conserving the physical quantity. To provide a full description for a new boson field, in
331 addition to the interaction term we introduce an invariant term for the kinetic energy of the bo-
332 son. Such approach allows us to derive the Lagrangian which is locally invariant with respect to
333 a certain gauge transformation and contains interacting fermions as well as interaction mediators.
334

335 The SM is a quantum field theory invariant under the local $SU(3)_C \times SU(2)_L \times U(1)_Y$ trans-
336 formation [7]. The SM Lagrangian includes all observed quantum fields and their interactions.
337

338 The part of the SM Lagrangian based on the $SU(3)_C$ symmetry and is called QCD or theory
339 of strong interactions. QCD has three types of charges which are called colors: red, blue, and
340 green. To be a subject of strong interaction, a fermion must posses a color charge. Quarks
341 and antiquarks are such fermions. The requirement to satisfy the gauge invariance with respect
342 to $SU(3)_C$ transformations generates eight massless gluons, and the non-abelian nature of the
343 $SU(3)$ group generates self-interactions of gluons including three-gluon and four-gluon vertices.
344

345 The part of the SM Lagrangian based on the $SU(2)_L \times U(1)_Y$ symmetry is a foundation of the
346 unified theory of electroweak interactions. $SU(2)_L$ reflects transformations in the weak isospin
347 space of left-handed fermions ([1], Ch. 9) while $U(1)_Y$ reflects transformations in a weak hyper-
348 charge space of all fermions. The requirement of the local gauge invariant generates four massless
349 vector bosons which are mediators of electromagnetic and weak interactions. The non-abelian
350 structure of $SU(2)$ group generates gauge boson self-couplings the same way as self-interactions
351 of gluons appear in QCD.
352

353 Mass terms for the vector bosons would violate the gauge invariance of the electroweak La-
354 grangian, however it is experimentally known that mediators of weak interactions are heavy
355 particles with masses $M_W = 80$ GeV and $M_Z = 91$ GeV. A possible solution of the discrepancy
356 is a mechanism of the spontaneous symmetry breaking.
357

358 The mechanism of the Spontaneous Symmetry Breaking and the appearance of the mass
359 terms for W and Z boson is realized by introducing an additional doublet of scalar fields. After
360 that, the Lagrangian is being transformed in such a way that W and Z bosons acquire masses
361 through their interactions with a new particle: a Higgs boson (H). A photon does not couple
362 to the Higgs boson remaining a massless particle and leaving QED symmetry group $U(1)$ to be
363 unbroken.
364

365 The measurement in this dissertation provides a test for the electroweak sector of the SM. We
366 will retrace the steps of the derivation of the EWK part of the SM Lagrangian starting from terms
367 of free fermions. The resulting Lagrangian accommodates electroweak gauge bosons including
368 their self-couplings. One of these self-couplings, $WW\gamma$, is the primary focus of our measurement.
369

370 It is experimentally known that dynamics of weak interactions depends on particle's chirality
371 ([1], chapter 4.4.1). In particular, a W boson couples to left-handed fermions and right-handed
372 antifermions only. Given different properties of left-handed and right-handed fermions, they
373 are treated differently by the electroweak theory. $SU(2)$ doublets are introduced for the wave
374 functions of left-handed fermions while $SU(2)$ singlets are introduced for the wave functions of
375 right-handed fermions. Equations 3 and 4 show wave functions for the first generation fermions.
376 Wave functions for the other two generations are constructed the same way.
377

$$\psi_1(x) = \begin{pmatrix} u \\ d' \end{pmatrix}_L, \psi_2(x) = u_R, \psi_3(x) = d'_R. \quad (3)$$

$$\psi_1(x) = \begin{pmatrix} \nu_e \\ e^- \end{pmatrix}_L, \psi_2(x) = \nu_{eR}, \psi_3(x) = e^-_R. \quad (4)$$

The state d' in Eq. 3 is a weak eigenstate which is a linear combination of mass eigenstates d, c and b quark's wave functions and is determined by the quark mixing matrix which is also called Cabibbo-Kobayashi-Maskawa matrix [7]:

381

$$\begin{pmatrix} d' \\ c' \\ b' \end{pmatrix} = V \begin{pmatrix} d \\ c \\ b \end{pmatrix} \quad (5)$$

To derive the unified electroweak Lagrangian, we start with the free fermion terms:

383

$$L_0 = \sum_{j=1}^3 i\bar{\psi}_j(x)\gamma^\mu\partial_\mu\psi_j(x), \quad (6)$$

where γ^μ are Dirac matrices ([1], chapter 7.1) and $\psi_j(x)$ are wave functions determined by Eqs. 3 and 4.

386

The wave function ψ_1 changes under the $SU(2)_L \times U(1)_Y$ transformations in the following way:

389

$$\psi_1(x) \rightarrow e^{iy_1\beta}U_L\psi_1(x), \quad (7)$$

while the wave functions $\psi_{(2,3)}(x)$ are singlets of $SU(2)_L$ and are affected only by $U(1)$ transformations:

392

$$\psi_{(2,3)}(x) \rightarrow e^{iy_{(2,3)}\beta}\psi_{(2,3)}(x). \quad (8)$$

The transformation in the weak isospin space is defined as $U_L \equiv e^{i\sigma_i\alpha_i/2}$ where σ_i are Pauli matrices ([1], chapter 4.2.2). Phases $\alpha_i(x)$ and $\beta(x)$ in Eqs. 7 and 8 are arbitrary functions of x , and $y_{(1,2,3)}$ are weak hypercharges which are named analogous to electric charges in QED.

396

In order to satisfy the local $SU(2)_L \times U(1)_Y$ invariance, partial derivatives in Eq. 6 have to be substituted with covariant derivatives:

399

$$D_\mu\psi_1(x) = [\partial_\mu - ig\tilde{W}_\mu(x) - ig'y_1B_\mu(x)]\psi_1(x) \quad (9)$$

$$D_\mu\psi_{(2,3)}(x) = [\partial_\mu - ig'y_{(2,3)}B_\mu(x)]\psi_{(2,3)}(x) \quad (10)$$

where g, g' are arbitrary constants,

401

$$\tilde{W}_\mu(x) \equiv \frac{\sigma_i}{2}W_\mu^i(x) = \frac{1}{\sqrt{2}} \begin{pmatrix} \sqrt{2}W_\mu^3 & (W_\mu^1 - iW_\mu^2)/\sqrt{2} \\ ((W_\mu^1 + iW_\mu^2)/\sqrt{2} & -W_\mu^3 \end{pmatrix}, \quad (11)$$

$B_\mu, W_\mu^1, W_\mu^2, W_\mu^3$ are four vector bosons that arise from the requirement of the Lagrangian to be invariant under local $SU(2)_L \times U(1)$ transformations.

404

405 The Lagrangian becomes:

406

$$L_0 \rightarrow L = \sum_{j=1}^3 i\bar{\psi}_j(x)\gamma^\mu D_\mu \psi_j(x) \quad (12)$$

407 To make new vector bosons physical fields it is necessary to add terms for their kinetic energies:

408

$$L_{KIN} = -\frac{1}{4}B_{\mu\nu}B^{\mu\nu} - \frac{1}{4}W_{\mu\nu}^i W_i^{\mu\nu} \quad (13)$$

409 where $B_{\mu\nu} \equiv \partial_\mu B_\nu - \partial_\nu B_\mu$, $W_{\mu\nu}^i \equiv \partial_\mu W_\nu^i - \partial_\nu W_\mu^i + g\epsilon^{ijk}W_\mu^j W_\nu^k$

410

411 Off-diagonal terms of \tilde{W}_μ are wave functions of charged vector bosons $W^\pm = (W_\mu^1 \mp iW_\mu^2)/\sqrt{2}$
 412 while W_μ^3 and B_μ are neutral fields which are mixtures of a Z boson and a photon determined by:

413

$$\begin{pmatrix} W_\mu^3 \\ B_\mu \end{pmatrix} \equiv \begin{pmatrix} \cos\theta_W & \sin\theta_W \\ -\sin\theta_W & \cos\theta_W \end{pmatrix} \begin{pmatrix} Z_\mu \\ A_\mu \end{pmatrix} \quad (14)$$

414 where θ_W is an electroweak mixing angle, A_μ is a photon field.

415

416 In order to be consistent with QED, terms involving A_μ in the electroweak Lagrangian must
 417 be equal to the corresponding terms in QED Lagrangian [7]:

418

$$L_{QED} = i\bar{\psi}(x)\gamma^\mu \partial_\mu \psi(x) - m\bar{\psi}(x)\psi(x) + qA_\mu(x)\bar{\psi}(x)\gamma^\mu \psi(x) - \frac{1}{4}F_{\mu\nu}(x)F^{\mu\nu}(x), \quad (15)$$

419 where q is electric charge of $\psi(x)$ field, $F_{\mu\nu} \equiv \partial_\mu A_\nu - \partial_\nu A_\mu$.

420

421 This requirement relates g , g' , θ_W and e as $g \sin\theta_W = g' \cos\theta_W = e$ and provides expression
 422 for weak hypercharges: $y = q - t_3$, where q is the electric charge and t_3 is a z -component of the
 423 weak isospin. This results in $y_1 = 1/6$, $y_2 = 2/3$, and $y_3 = -1/3$ for quarks and $y_1 = -1/2$,
 424 $y_2 = 0$, and $y_3 = -1$ for leptons. A right-handed neutrino has a weak hypercharge of $y_2 = 0$. It
 425 also does not have an electric charge and, as a right-handed fermion, has $t_3 = 0$ and, therefore,
 426 does not couple to a W boson. Thus, a right-handed neutrino does not participate in any SM
 427 interaction.

428

429 Writing \tilde{W}_μ in Eq. 13 explicitly, we obtain triple gauge coupling (TGC) and quartic gauge
 430 coupling (QGC) terms:

431

$$L_{TGC} = -\frac{g}{4}(\partial_\mu W_\nu^i - \partial_\nu W_\mu^i)\epsilon^{ijk}W^{\mu j}W^{\nu k} - \frac{g}{4}\epsilon^{ijk}W_\mu^j W_\nu^k(\partial^\mu W^{\nu i} - \partial^\nu W^{\mu i}) \quad (16)$$

$$L_{QGC} = -\frac{g^2}{4}\epsilon^{ijk}\epsilon^{ilm}W_\mu^j W_\nu^k W^{\mu l}W^{\nu m} \quad (17)$$

432 Substituting W_μ^i and B_μ in Eq. 16 and Eq. 17 with the wave functions of W^\pm , Z and a photon:

433

$$B_\mu = -\sin\theta_W Z_\mu + \cos\theta_W A_\mu, W_\mu^3 = \cos\theta_W Z_\mu + \sin\theta_W A_\mu, \quad (18)$$

$$W_\mu^1 = \sqrt{2}(W^+ + W^-), W_\mu^2 = \sqrt{2}(W^- + W^+), \quad (19)$$

434 we receive charged TGC and QGC terms in the Lagrangian (those involving two or four W
 435 bosons) in the forms of Eqs. 20 and 23, but all neutral TGC and QGC terms (those not involv-
 436 ing any W bosons) cancel out.

437

438 Equation 20 involves WWZ (Eq. 21) and $WW\gamma$ (Eq. 22) interactions:

439

$$L_{TGC} = L_{TGC}^{(1)} + L_{TGC}^{(2)}, \quad (20)$$

$$L_{TGC}^{(1)} = -ie \cot \theta_W (W^{-\mu\nu} W_\mu^+ Z_\nu - W^{+\mu\nu} W_\mu^- Z_\nu + W_\mu^- W_\nu^+ Z^{\mu\nu}), \quad (21)$$

$$L_{TGC}^{(2)} = -ie (W^{-\mu\nu} W_\mu^+ A_\nu - W^{+\mu\nu} W_\mu^- A_\nu + W_\mu^- W_\nu^+ A^{\mu\nu}). \quad (22)$$

440 Equation 23 involves $WWWW$ (Eq. 24), $WWZZ$ (Eq. 25), $WWZ\gamma$ (Eq. 26), and $WW\gamma\gamma$
 441 (Eq. 27) interactions:

442

$$L_{QGC} = L_{QGC}^{(1)} + L_{QGC}^{(2)} + L_{QGC}^{(3)} + L_{QGC}^{(4)}, \quad (23)$$

$$L_{QGC}^{(1)} = -\frac{e^2}{2 \sin^2 \theta_W} (W_\mu^+ W^{-\mu} W_\nu^+ W^{-\nu} - W_\mu^+ W^{\mu+} W_\nu^- W^{-\nu}), \quad (24)$$

$$L_{QGC}^{(2)} = -e^2 \cot^2 \theta_W (W_\mu^+ W^{-\mu} Z_\nu Z^\nu - W_\mu^+ Z^\mu W_\nu^- Z^\nu), \quad (25)$$

$$L_{QGC}^{(3)} = -e^2 \cot \theta_W (2W_\mu^+ W^{-\mu} Z_\nu A^\nu - W_\mu^+ Z^\mu W_\nu^- A^\nu - W_\mu^+ A^\mu W_\nu^- Z^\nu), \quad (26)$$

$$L_{QGC}^{(4)} = -e^2 (W_\mu^+ W^{-\mu} A_\nu A^\nu - W_\mu^+ A^\mu W_\nu^- A^\nu). \quad (27)$$

443 In the measurement of this dissertation we probe $WW\gamma$ coupling (Eq. 22).

444

445 The unified electroweak Lagrangian discussed above involves kinetic energy terms for fermions
 446 and gauge bosons as well as interactions of fermions with gauge bosons, TGC, and QGC. How-
 447 ever, this Lagrangian does not contain any mass terms. Because left-handed and right-handed
 448 wave functions transform differently under the electroweak symmetry, adding fermion mass terms
 449 of $\frac{1}{2}m_f^2 \bar{\psi}\psi$ would violate the Lagrangian invariance and, therefore, fermion mass terms are for-
 450 bidden by the $SU(2) \times U(1)$ symmetry requirement. Mass terms for gauge bosons also would
 451 violate the Lagrangian invariance just as a photon mass term $\frac{1}{2}m^2 A^\mu A_\mu$ would violate $U(1)$
 452 invariance of L_{QED} [1]. Therefore, Lagrangian L in Eq. 12 contains massless particles only.

453

454 However, it is known from experiments that a Z boson, a W boson and fermions are massive
 455 particles and, therefore, our theory should accommodate their masses. To introduce masses into
 456 the electroweak Lagrangian, an $SU(2)_L$ doublet of complex scalar fields $\phi(x)$ is added to the
 457 Lagrangian:

458

$$\phi(x) \equiv \begin{pmatrix} \phi^{(+)}(x) \\ \phi^{(0)}(x) \end{pmatrix} \quad (28)$$

459 By selecting a special gauge of $\phi(x)$ it is possible to spontaneously break electroweak sym-
 460 metry, generate a new scalar particle, a Higgs boson [7], and introduce mass terms for W and
 461 Z bosons and charged fermions through their couplings to the Higgs boson. The strength of the
 462 coupling constant is proportional to the square of the particle's mass, therefore, heavier particles
 463 are more likely to interact with H , and massless particles do not couple to H .

464

465 The mechanism of generating a fermion's mass involves both left-handed and right-handed
 466 components of the fermion. If our hypothesis that right-handed neutrinos do not exist is right,
 467 then the Higgs mechanism does not generate neutrino masses. However, from the experiments
 468 of neutrino oscillations, neutrinos are known to have masses even though they are orders of
 469 magnitude smaller than those of other fermions. Several hypotheses were offered to resolve this

⁴⁷⁰ contradiction however at the moment the mechanism of neutrinos to acquire masses remain un-
⁴⁷¹ known [5].

⁴⁷² In this dissertation, we study an electroweak process $W\gamma \rightarrow l\nu_l\gamma$, more specifically, probe
⁴⁷³ TGC vertex $WW\gamma$ (Eq. 22). To do that, we are measuring a differential cross section with
⁴⁷⁴ respect to the photon transverse momentum. The concept of the cross section in particle physics
⁴⁷⁵ is discussed in the next chapter.

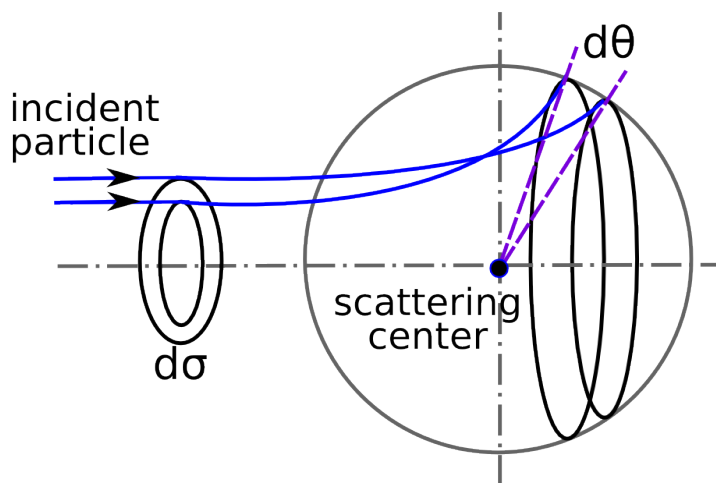
⁴⁷⁶

⁴⁷⁷

478 2.2 Cross Section and Luminosity

479 In this dissertation we are measuring the total cross section of the process $pp \rightarrow l\nu\gamma + X$ and
 480 its differential cross section in transverse momentum of the photon. A cross section in particle
 481 physics is an interaction probability per unit flux of incident particles [12]. It can be interpreted
 482 as an area which must be crossed by an incident particle in order to interact with a scattering
 483 center, or, in case of a differential cross section, area $d\sigma$ within which an incident particle must
 484 appear to be scattered off by an angle $d\theta$ (Fig. 8). The relationship between $d\sigma$ and $d\theta$ gives us
 485 the expression for a differential cross section $d\sigma/d\theta$. Integrating over $d\theta$, we obtain the total cross
 486 section σ . The cross section concept illustrated in Fig. 8 is generalized to be an effective area,
 487 and is generalized for two (or more) particle interactions rather than a light particle scattering
 488 off a stationary center.

489 The angle θ here is used only as an illustration of a concept of differential cross section. In
 490 particle physics we measure a differential cross section with respect to a parameter X which can
 491 be a parameter of one of final state particles or of a system of final state particles. For example,
 492 a transverse momentum of a final state photon P_T^γ , an invariant mass of two final state leptons
 493 m_{ll} , a number of jets associated with the process N_{jets} and other parameters.



496 Figure 8: Illustration of the differential cross section concept in the classical case.
 497

498 In the scenario illustrated in Fig. 8, the number of particles passing through the area σ per
 499 unit time is $N = L \cdot \sigma$, where L is the flux of incident particles and is called luminosity. For
 500 colliding beams, the luminosity is determined by collisions frequency, the number of colliding
 501 particles in each beam, and beams cross sections. The cross section σ of a specific process can
 502 be determined from an experiment as $\sigma = N/L$.

503 A cross section can be computed theoretically using the following expression:

$$\sigma = \frac{W_{fi}}{F} N_{fs}, \quad (29)$$

504 where W_{fi} is a transition probability between final and initial states of the system per unit spatial
 505 volume, F is the initial flux, and N_{fs} is the density of final states ([8], chapter 4.3). The initial
 506 flux in this expression is determined as number of incident particles per unit volume multiplied

507 by their velocity and multiplied by number of target particles per unit volume.

508

509 The formula of the cross section relevant for our measurement, two particles to three final
510 state particles scattering $1 + 2 \rightarrow 3 + 4 + 5$, is determined by the Fermi's Golden Rule [1]:

511

$$\sigma = \frac{1}{4\sqrt{(p_1 p_2)^2 - (m_1 m_2)^2}} \int |M|^2 (2\pi)^4 \delta^4(p_1 + p_2 - p_3 - p_4 - p_5) \prod_{j=3}^5 \frac{1}{2\sqrt{\bar{p}_j^2 + m_j^2}} \frac{d^3 \bar{p}_j}{(2\pi)^3}, \quad (30)$$

512 where p_i are four-momenta and \bar{p}_i are three momenta of the initial state and the final state
513 particles, m_i are masses of particles, M is the process amplitude determined by the dynamics
514 of the particles interaction. All available momenta of the final state particles is called the phase
515 space.

516

517 During proton-proton collisions, at high energy the hard scattering process occurs between
518 partons in the protons, as discussed in Ch. 1.4. Therefore, the cross section of a process
519 $pp \rightarrow X + Y$ has two ingredients: PDFs and a partonic cross section $\sigma_{ab \rightarrow X}$. The partonic
520 cross section is described by perturbative QCD while PDFs require non-perturbative computa-
521 tions and are determined, in part, from experiments (Fig. 7). According to the QCD factorization
522 theorem [9]:

523

$$\sigma(pp \rightarrow X + Y) = \sum_{a,b} \int dx_a dx_b f_a(x_a, Q^2) f_b(x_b, Q^2) \sigma(ab \rightarrow X). \quad (31)$$

524 In the case of $W\gamma$ process, X is $l\nu\gamma$, ab are $q_i\bar{q}_j$ or $q_j\bar{q}_i$. Q^2 is the large momentum scale
525 that characterizes hard scattering, f_a and f_b are PDFs, x_a and x_b are fractions of momenta of
526 the partons. In the next sections we will discuss the computation of partonic cross sections of
527 the $W\gamma$ process and possible BSM effects.

528

2.3 Standard Model $W\gamma$ Production

A W boson in proton-proton collisions can be produced in the processes $q\bar{q}' \rightarrow W$ where q and \bar{q}' are a quark and an antiquark which have a total charge of +1 if producing a W^+ boson or -1 if producing a W^- boson. The processes $u\bar{d} \rightarrow W^+$ and $d\bar{u} \rightarrow W^-$ are the most likely to occur because u and d are valence quarks in a proton. There are twice as many u quarks in a proton as d quarks, therefore, W^+ is produced twice more frequently than W^- . Antiquarks \bar{d} and \bar{u} come from sea $q\bar{q}$ pairs of the other proton.

One created, a W boson decays immediately and in an experiment one detects its decay products rather than the W boson itself. Decay modes of a W boson include $W^\pm \rightarrow l^\pm \nu_l (\bar{\nu}_l)$ where $l^\pm = e^\pm, \mu^\pm$ or τ^\pm with branching fractions of 11% per a leptonic channel [5]. The remaining 67% account for various $W \rightarrow q\bar{q}'$ decays. In this dissertation we only consider $W^\pm \rightarrow \mu^\pm \nu_\mu (\bar{\nu}_\mu)$ and $W^\pm \rightarrow e^\pm \nu_e (\bar{\nu}_e)$ channels.

A photon can be emitted from any charged particle of the process: a quark, an antiquark, a charged lepton or a W boson (Fig. 9, top). A quark and an antiquark are initial state particles and, therefore, if one of them radiates a photon, we call such process the initial state radiation (ISR). A muon or an electron is a final state particle and if it radiates a photon, we call such process the final state radiation (FSR). Finally, a W boson is a gauge boson and if it radiates a photon, the process has a vertex with three gauge bosons: $WW\gamma$, and we call such process the triple gauge coupling (TGC). We cannot distinguish between these processes experimentally because we detect final state particles only.

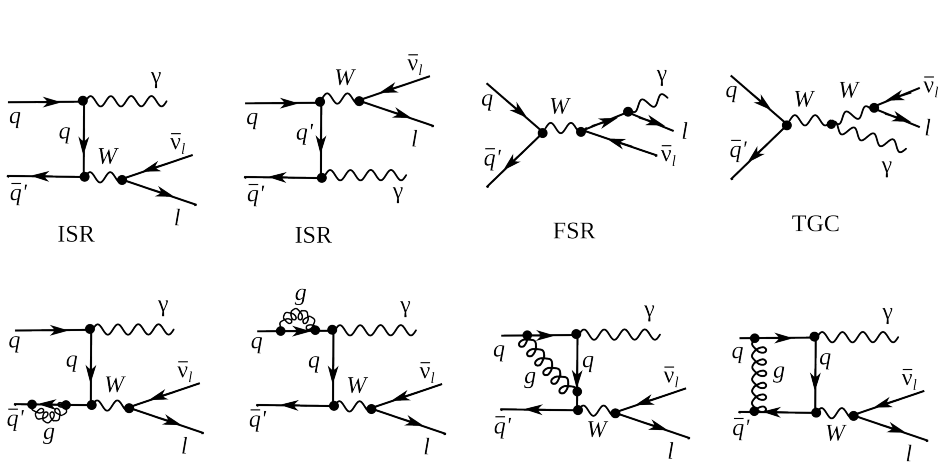


Figure 9: Feynman diagrams of $W\gamma$ production. Top: LO diagrams, bottom: several examples of NLO in QCD.

The electroweak Lagrangian is described in Chapter 2.1. It is possible to derive equations of motion from the Lagrangian for any fields involved [1]. However, in a quantum field theory equations of motion cannot be solved exactly and, therefore, the perturbative approach is used if a coupling constants is $g \ll 1$.

To represent the process graphically Feynman diagrams were invented. Also the diagrams can be used to calculate the process amplitude M from Eq. 30 because they are determined by Lagrangian terms relevant to the process. There is infinite number of Feynman diagrams corresponding to any specific process and the total amplitude of the process is a sum of individual amplitudes of each diagram and it is not technically possible to take into account all of them. Each vertex introduces a factor in the amplitude of the process that is proportional to

563 the coupling constant. If the coupling constant is $g \ll 1$, the perturbative approach arranges
564 all the diagrams by orders of contribution, and, therefore, the Feynman diagrams with fewer
565 vertices would give a significantly larger contribution to the amplitude. In Fig. 9 examples of
566 the Leading Order (LO) and the Next-to-Leading Order (NLO) Feynman diagrams are shown
567 (top and bottom diagrams respectively).

568

569 At LO, the $W\gamma$ process is represented by four Feynman diagrams including one FSR, one
570 TGC and two ISR diagrams. Each LO diagram has three vertices. The first calculation of the
571 $W\gamma$ process with necessary expressions can be found in [14].

572

573 The NLO corrections to the amplitude of the $W\gamma$ process that are shown in Fig. 9 are QCD
574 corrections only, which include gluon loops at the same quark line and exchange of a gluon be-
575 tween two different quark lines, however, QED and weak NLO diagrams are also possible. QED
576 corrections involve radiations of extra photons by charged particles, exchange of photons be-
577 tween different charged particles or a photon can be radiated and absorbed by the same charged
578 particle forming a loop. Similarly, weak corrections involve extra virtual W or Z bosons. The
579 QCD corrections are the largest among the discussed correction types because the QCD coupling
580 constant is the largest.

581

582 A theoretical cross section in particle physics is compared to a measurement result thus test-
583 ing the predictions of the model as well as the theoretical cross section is used for producing a
584 simulation. In a simulation, a large set of pp collisions resulting in a physics process of interest
585 is modeled creating a data set that mimics real data. A typical simulation consists of two parts:
586 the generation of the process and the simulation of particles paths through the detector. The
587 first stage contains a collection of events with final state particles with kinematic quantities dis-
588 tributed according to theoretical predictions for a given process. This stage relies on the theory
589 including the cross section and also all dynamics of the process. The second stage simulates
590 the interaction with media during propagation of particles through the model of the detector as
591 well as the response of detector electronics. In its final form, a simulated dataset has the same
592 format and content of detector signals for each event as real data, and can undergo the same
593 reconstruction and analysis procedure as real data would.

594

595 The most precise theoretical $W\gamma$ cross section available is the Next-to-Next-to-Leading Order
596 (NNLO) cross section in QCD [15]. The effects of the NNLO correction over the NLO correction
597 and over the LO result are shown in Fig. 10 for the transverse mass of the final state particles
598 $m_T^{l\nu\gamma}$ and for the rapidity difference between a charged lepton and a photon $\Delta_{l\gamma}$. The NNLO and
599 NLO theoretical predictions for the photon transverse momentum p_T^γ are overlaid with 7 TeV
600 ATLAS result. The contribution from higher order corrections is estimated to be $\pm 4\%$. However,
601 the NNLO theoretical result was published only recently, in 2015, and no NNLO $W\gamma$ simulation
602 is available at this time. The simulation used in this analysis is LO + up to two hadronic jets
603 simulation which was found to give the same predictions as the NLO result.

604

605 Certain BSM theories predict an enhancement of the contribution from the TGC diagram
606 over the SM prediction. The discussion of these BSM effects and how they affect the $W\gamma$ process
607 takes place in Ch. 2.4.

608

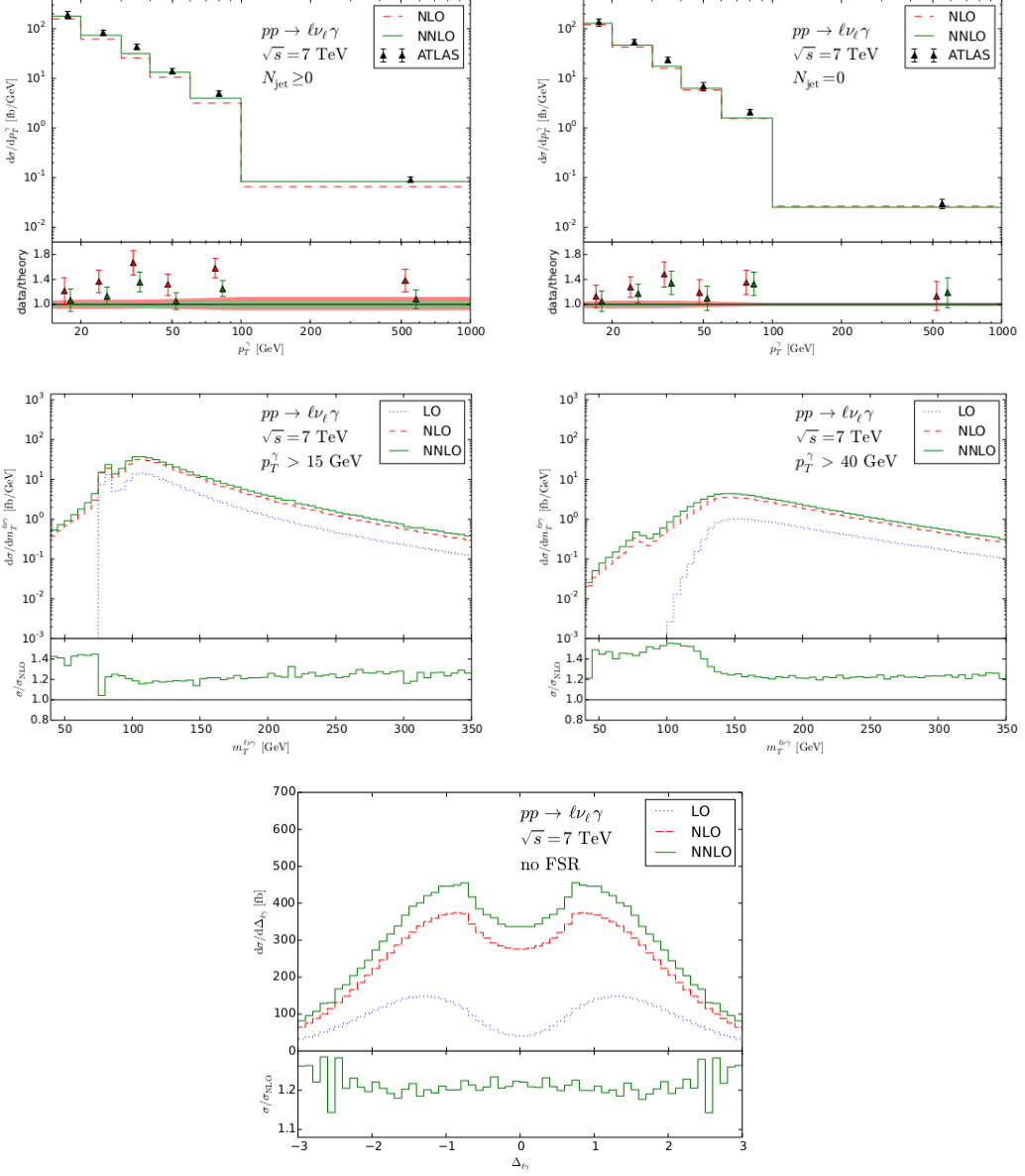


Figure 10: Theory spectra.

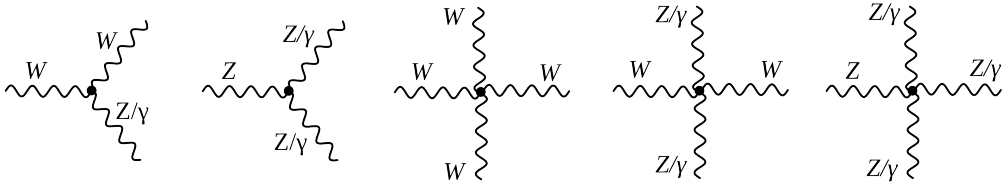
609 2.4 Anomalous $W\gamma$ Production

610 Most BSM physics theories predict the existence of particles with masses lying beyond the dis-
 611 covered energy range. If their masses are not accessible even at the accelerators with the highest
 612 energies, the direct detection of such particles is not possible. However, loops of heavy particles
 613 can affect diagrams of productions of lighter particles. They would give additional contributions
 614 to TGC and QGC couplings and, therefore, to the amplitudes to the processes involving TGC
 615 and QGC productions. There would be a different number of events produced in the process
 616 than one can expect based on SM predictions as shown in Fig. 12.

617

618 TGC and QGC couplings can be probed by precision measurements of SM processes of diboson
 619 and triboson productions because these processes can occur through TGC and QGC. TGC
 620 and QGC are represented by vertices with three and four bosons (Fig. 11). As discussed in
 621 Ch. 2.1, charged TGC and QGC are possible at tree level in the SM while neutral TGC and
 622 QGC are not.

623



624 Figure 11: Charged TGC (first), neutral TGC (second), charged QGC (third and fourth), and
 625 neutral QGC (fifth) vertices.

626 To account for the effects from the potential loops of heavy particles, we introduce an ef-
 627 fective Lagrangian with arbitrary values of coupling constants which can be reduced to the SM
 628 Lagrangian if these constants would have their SM values. Introducing the effective Lagrangian
 makes searches model-independent because we do not specify particles that form the loops but
 instead just check whether there is a deviation from the SM prediction in measured observables.

629

630 In $W\gamma$ measurement we can probe $WW\gamma$ vertex. The most general Lorentz invariant La-
 631 grangian terms of $WW\gamma$ interaction takes the following form [17]:

632

$$633 iL_{eff}^{WW\gamma} = iL_{eff(1)}^{WW\gamma} + iL_{eff(2)}^{WW\gamma} + iL_{eff(3)}^{WW\gamma}, \quad (32)$$

634 where

$$iL_{eff(1)}^{WW\gamma} = e[g_1^\gamma A^\mu (W_{\mu\nu}^- W^{+\nu} - W_{\mu\nu}^+ W^{-\nu}) + \kappa_\gamma W_\mu^+ W_\nu^- A^{\mu\nu} + \frac{\lambda_\gamma}{m_W^2} A^{\mu\nu} W_\nu^{+\rho} W_{\rho\mu}^-], \quad (33)$$

$$iL_{eff(2)}^{WW\gamma} = e[i g_5^\gamma \epsilon_{\mu\nu\rho\sigma} ((\partial^\rho W^{-\mu}) W^{+\nu} - W^{-\mu} (\partial^\rho W^{+\nu})) A^\sigma + i g_4^\gamma W_\mu^- W_\nu^+ (\partial^\mu A^\nu + \partial^\nu A^\mu)], \quad (34)$$

$$iL_{eff(3)}^{WW\gamma} = e[\frac{\tilde{\kappa}_\gamma}{2} W_\mu^- W_\nu^+ \epsilon^{\mu\nu\rho\sigma} A_{\rho\sigma} - \frac{\tilde{\lambda}_\gamma}{2m_W^2} W_{\rho\mu}^- W_\nu^{+\mu} \epsilon^{\nu\rho\alpha\beta} A_{\alpha\beta}], \quad (35)$$

635 where e is the absolute value of the electron charge, A^μ is the photon field, $W^{\pm\mu}$ are fields of
 636 W^\pm bosons, $W_{\mu\nu} = \partial_\mu W_\nu - \partial_\nu W_\mu$, $A_{\mu\nu} = \partial_\mu A_\nu - \partial_\nu A_\mu$, m_W is the mass of a W boson, g_1^γ , κ_γ ,

637 λ_γ , g_5^γ , g_4^γ , κ_γ , and $\tilde{\lambda}_\gamma$ are constants.
 638

639 Despite seven constants in the extended Lagrangian, only λ_γ and κ_γ are considered in the
 640 aTGC searches. The rest of the constants are fixed to their SM values based on the following
 641 considerations. The constants $g_1^\gamma = 1$ and $g_5^\gamma = 0$ are fixed to make the Lagrangian obey the
 642 electromagnetic gauge invariance for the on-shell photons. The non-zero value of g_5^γ also violates
 643 C and P conservations, and non-zero values of g_4^γ , κ_γ , $\tilde{\lambda}_\gamma$ violate the CP conservation law. Such
 644 violation parametrizations are not considered in charged TGC measurements, thus, constants
 645 g_4^γ , κ_γ , and $\tilde{\lambda}_\gamma$ are fixed to zero.
 646

647 The SM values of λ_γ and κ_γ are $\lambda_\gamma = 0$ and $\kappa_\gamma = 1$. For convenience, the deviation from the
 648 SM value is introduced $\Delta\kappa_\gamma \equiv \kappa_\gamma - 1$. These two parameters are tested in $WW\gamma$ aTGC searches
 649 because non-zero values of these parameters would not violate any fundamental law.
 650

651 The most significant effects of aTGC would appear at high energy scales. Figure 12 shows
 652 this effect in P_T^γ spectrum of 7 TeV $W\gamma \rightarrow \mu\nu\gamma$ measurement. As seen in Fig. 12 the spectrum
 653 with non-zero values of aTGC constants at low P_T^γ coincides with the SM prediction but for
 654 higher P_T^γ the disagreement appears.
 655

656 A common approach to aTGC searches is measuring a spectrum of a kinematic parameter
 657 highly correlated with an energy of a final state particle or a system of final state particles. For
 658 $W\gamma$ process, the most sensitive variable is P_T^γ . Examining this spectrum allows us to probe and
 659 constrain aTGC coupling constants. Chapter 2.5 reviews the experimental results to date on
 660 constraining aTGC coupling constants of $WW\gamma$ vertex.
 661

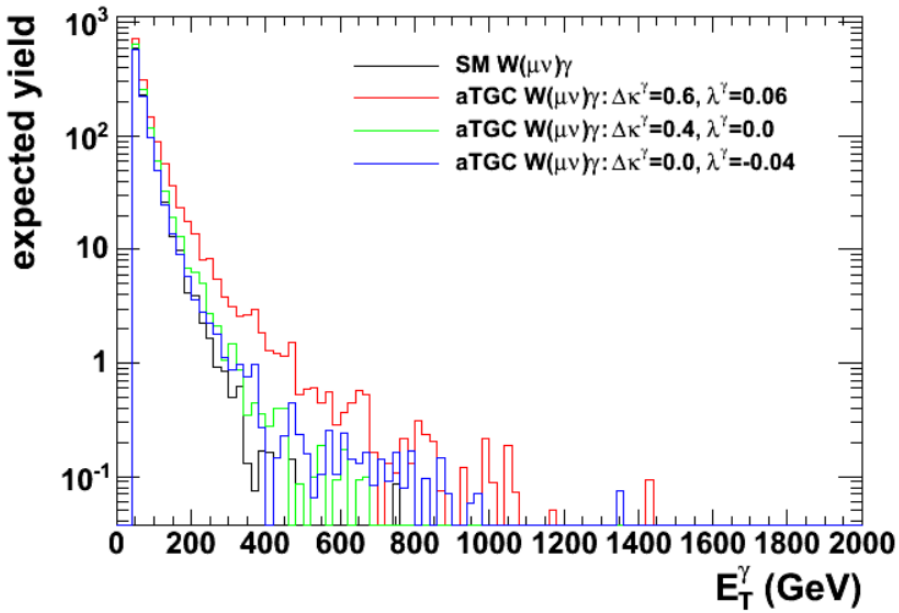


Figure 12: Distributions of P_T^γ of simulated $W\gamma \rightarrow \mu\nu\gamma$ events with different values of aTGC constants at LHC energy of $\sqrt{s} = 7$ TeV. Source of figure: [18].

662 2.5 Measurements in the Past

663 ATGC parameters of $WW\gamma$ vertex can be probed in measurements of $W\gamma$, WW , WZ processes.
 664 Limits on $\Delta\kappa_\gamma$ and λ_γ constants obtained by different experiments are summarized in Fig. 13.
 665 The summary include the combination results from D0 [19] and LEP [20] as well as results of
 666 several individual measurements by ATLAS and CMS including $W\gamma$ at $\sqrt{s} = 7$ TeV [21], [22],
 667 WW at $\sqrt{s} = 7$ and 8 TeV [23], [24], [25], and WV at $\sqrt{s} = 7$ and 8 TeV [26], [28] measurements.
 668

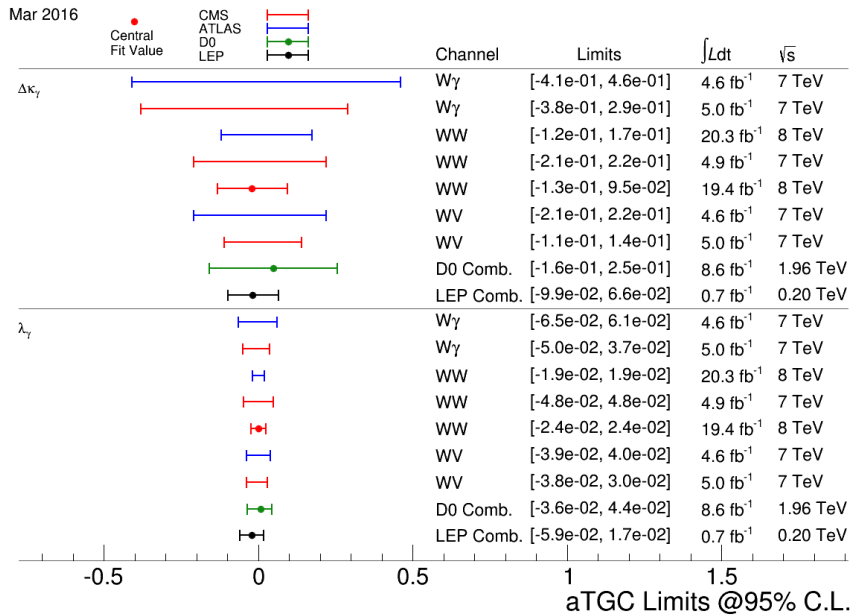


Figure 13: Summary of limits on the $WW\gamma$ aTGC coupling constants. Figure from [27].

669 The most recent measurements of $W\gamma$ production were performed by CMS [22] and AT-
 670 LAS [21] collaborations with pp collisions at $\sqrt{s} = 7$ GeV collected in 2011. Both collaborations
 671 considered two channels: $W\gamma \rightarrow \mu\nu\gamma$ and $W\gamma \rightarrow e\nu\gamma$.
 672

673 Dibosons processes are rare in pp -collisions and analysts have to filter out events of their
 674 interest from many processes which are more likely to happen. To do that, variety of selection
 675 criteria is applied which reject most of background events increasing a signal fraction in the
 676 selected sample as much as possible. However, even after all possible selection criteria are ap-
 677 plied, majority of selected events are still background events and it is not possible to reduce the
 678 background any further without also significantly reducing signal.
 679

680 The major source of such irreducible background is the fake photon background where
 681 hadronic jets are misidentified as photons. Such events originate from mostly $W+jets$ pro-
 682 cess but $Z+jets$ and $t\bar{t}+jets$ events contribute to this source of the background as well. In the
 683 electron channel there is one more significant background that is the fake photon background
 684 where electron is misidentified as a photon. Such events are coming from $Z+jets$ events. For the
 685 muon channels this background is small. Other sources of backgrounds for both channels include
 686 real- γ , fake lepton + real photon and fake lepton + fake photon backgrounds. The major source
 687 of real- γ background is $Z\gamma$ process where a final state lepton and a photon mimics $W\gamma$ final state,
 688 fake lepton + real photon background originates from $\gamma+jets$ process where a jet is misidentified
 689 as a lepton and fake lepton + fake photon backgrounds comes from dijets and multijets events
 690 where one of the jets is misidentified as a lepton and the other one is misidentified as a photon.
 691 The probability of a jet to be misidentified as a lepton is very small, therefore, fake lepton +
 692 real photon and fake lepton + fake photon backgrounds are negligible.

693 Both channels provide measurements of P_T^γ spectra because this variable is the most sensitive
 694 to the potential aTGC. The P_T^γ spectra of the selected events in data superimposed with selected
 695 events in the simulation of the signal and estimated background contribution for the muon and
 696 electron channels are shown in Fig. 14 for CMS and in Fig. 15 for ATLAS measurement. Both
 697 measurements show a good agreement between data and the simulation.
 698

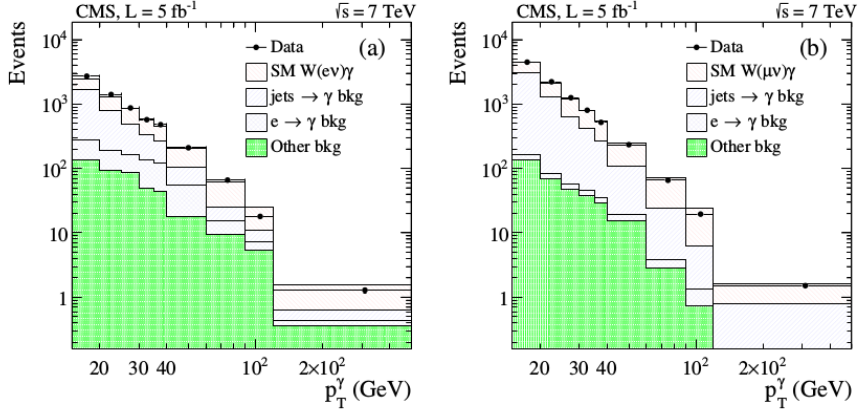


Figure 14: The distribution fo the p_T^γ of $W\gamma$ candidates in the analysis of 7 TeV CMS data. Data vs signal MC + background estimates. Left: $W\gamma \rightarrow e\nu\gamma$, right: $W\gamma \rightarrow \mu\nu\gamma$ [22].

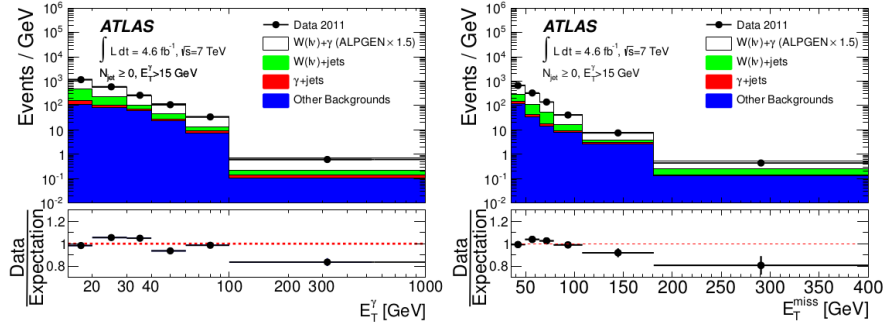


Figure 15: The distribution of the photon transverse momentum (left) and missing transverse momentum (right) of $W\gamma$ candidates in the analysis of 7 TeV ATLAS data. Data vs signal MC + background estimates [21].

700 The phase space restrictions of $W\gamma$ measurements come from the considerations of the detec-
 701 tor acceptance, reducing heavily background-dominated regions and theoretical considerations
 702 such as to avoid divergence of the cross section and to reduce ISR and FSR contributions to the
 703 cross section.

704 CMS provides measurements of the P_T^γ spectrum, the total cross section within the phase
 705 spaces of $\Delta R > 0.7$, $P_T^\gamma > 15$ GeV, $P_T^\gamma > 60$ GeV and $P_T^\gamma > 90$ GeV.

706 ATLAS, in addition to the P_T^γ spectrum, total cross section and limits, provides the dif-
 707 ferential cross section and cross section with different number of associated jets. The phase

710 space restrictions for ATLAS measurement include requirements on charged lepton kinematics
711 $P_T^l > 25$ GeV, $|\eta_l| < 2.47$, requirements on the transverse momentum of a neutrino $P_T^\nu > 35$ GeV,
712 photon kinematics $P_T^\gamma > 15$ GeV, $|\eta^\gamma| < 2.37$, photon isolation fraction $\epsilon_h^P < 0.5$ and lepton-
713 photon separation $\Delta R(l, \gamma) > 0.7$. For the differential cross section by different number of the
714 associated jets, the requirements on jets kinematics and jets separation from lepton and photon
715 are also applied: $E_T^{jet} > 30$ GeV, $|\eta^{jet}| < 4.4$, $\Delta R(e/\mu/\gamma, jet) > 0.3$. No evidence of a new
716 physics is observed.

717
718 The estimated cross sections with any number of associated jets for $P_T^\gamma > 15$ GeV are
719 $\sigma(pp \rightarrow W\gamma \rightarrow l\nu\gamma) = 37.0 \pm 0.8$ (stat.) ± 4.0 (syst.) ± 0.8 (lumi.) pb and
720 $\sigma(pp \rightarrow W\gamma \rightarrow l\nu\gamma) = 2.77 \pm 0.03$ (stat.) ± 0.33 (syst.) ± 0.14 (lumi.) pb
721 for CMS and ATLAS respectively. The results agree with NLO MCFM predictions of $31.81 \pm$
722 1.8 pb for the phase space used by CMS and of 1.96 ± 0.17 pb for the phase space used by ATLAS.
723

724 In addition to the cross sections, both CMS and ATLAS provide limits on aTGC coupling
725 constants $\Delta\kappa_\gamma$ and λ_γ . To do that, samples with non-zero aTGC coupling constants are gen-
726 erated, run through the whole reconstruction and selection procedures, and compared to the
727 measured results of P_T^γ spectra. The results on one-dimensional limits are quoted in Fig. 13
728 while the results on two-dimensional limits can be found in [21], [22].
729

730 In this dissertation we are measuring total and differential $d\sigma/dP_T^\gamma$ cross section. While the
731 aTGC limits are not derived in this dissertation, the measured differential cross section can be
732 used to derive them. The measurement details and results are described in Chapter 5.
733

734 **3 Experimental Setup**

735 3.1 Large Hadron Collider

736 The Large Hadron Collider (LHC) [31], [32], [33] is the largest particle accelerator and the most
 737 ambitious research facility ever built. The LHC is placed into a tunnel originally built for the LEP
 738 accelerator. The LEP was decommissioned to make room for the LHC. The tunnel is about 27 km
 739 in circumference, located at the Swiss-French boundary up to 100 meters undergroud.

740 Before entering LHC, particle beams are going through several stages of the acceleration and
 741 the LHC is the last element of the chain of the CERN's accelerator complex (Fig. 16). Protons
 742 are extracted from hydrogen atoms, are accelerated by Linac2 to energies of 5 MeV, then injected
 743 into the Proton Synchrotron Booster (PSB) where they reach energies of 1.4 GeV. After that
 744 protons are sent to PS and Super PS (SPS) where they are accelerated up to 25 GeV and 450 GeV
 745 respectively. Finally, protons enter the LHC and are accelerated to reach their collision energies
 746 of several TeV per beam. Besides protons, the complex also accelerates and collides lead ions
 747 however in this dissertation we analyze data from proton-proton collisions only and, therefore,
 748 are not discussing lead ion collisions.

750 Main goals of LHC were to detect the SM Higgs boson if it existed and to search for evidences
 751 of BSM physics which may give a clue on understanding the phenomena including but not limited
 752 to the dark matter, the matter-antimatter asymmetry, the nature of the gravitational force. Six
 753 detectors are installed at the LHC to detect particles and perform the relevant measurements.
 754 There are general purpose detectors ATLAS and CMS, there is LHCb which specializes of the
 755 physics of B-mesons, and ALICE which is designed to detect products of heavy ion collisions. In
 756 addition, there are two relatively small detectros: LHCf and TOTEM which are installed close
 757 to the ATLAS and CMS collision points respectively.

759 A new particle with mass $m = 125$ GeV was discovered by the CMS [3] and the ATLAS [4]
 760 collaborations in 2012. The particle is consistent with the SM Higgs boson predicted by the
 761 EWK sector of the SM. The discovery of the Higgs boson is the greatest achievement by the
 762 LHC to date.

764 While different BSM searches have been constituting a significant part of the LHC physics
 765 program since the beginning of its operation, no deviations from the SM were found by any of
 766 the experiments. The searches continue with higher beam energies and larger amount of data.

768 The design energy of the LHC is 7 TeV per beam however several lower energy points were
 769 and are being probed. In 2010-2011 the LHC operated at energy of 3.5 TeV per beam which was
 770 already higher than energy of any other collider. In 2012 the energy increased up to 4 GeV. In
 771 2013-2014 the LHC was shut down for upgrades. Collisions were restarted at 6.5 TeV in 2015
 772 and the LHC is still operating at this energy in 2016.

774 All important measurements performed at lower energies are also repeated at higher energies
 775 because the ability to probe higher energy scales increases our chances for a discovery and even
 776 if no deviations from the known physics are found at a given energy point, the discovery is still
 777 possible to happen as we go higher in the energy.

779 In addition to the beam energy, there are many other collider parameters. A brief summary
 780 of them is available in Tab. 2. One of the most important parameters of an accelerator is the
 781 ability to produce a large number of interesting collisions which is determined by the luminosity.
 782 The instantaneous luminosity is determined by the following expression [5]:

$$785 L = f \frac{n_1 n_2}{4\pi \sigma_x \sigma_y}$$

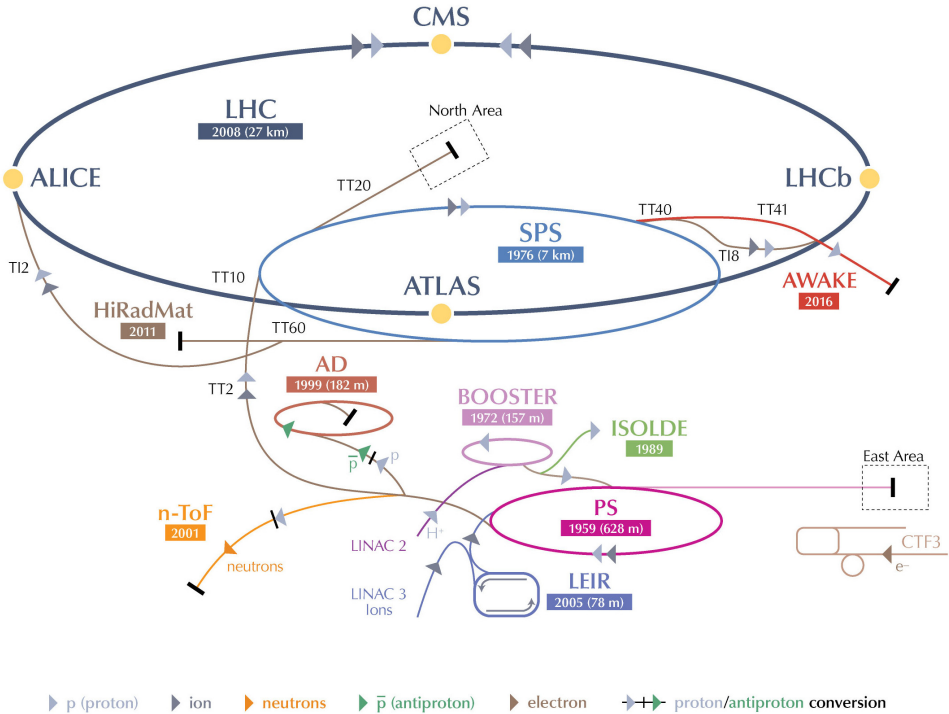
786 where n_1 and n_2 are numbers of particles in colliding bunches, f is a frequency of collisions,
 787 σ_x and σ_y are beam sizes in horizontal and vertical directions. To determine the integrated
 788 luminosity, one has to integrate the instantaneous luminosity over time:

$$L_{int} = \int L dt$$

The luminosity of the LHC is also higher than of any previously existed collider. The integrated luminosity of the LHC for different years of the operation are shown in Fig. 17. Run periods of LHC in 2010-2012 refer to Run I of the LHC operation. While working on energy of $\sqrt{s} = 7$ TeV, LHC delivered 44.96 pb^{-1} and 6.1 fb^{-1} of data in 2010 and 2011 year respectively. In 2012 the working energy of LHC was $\sqrt{s} = 8$ TeV, and the integrated luminosity was $L_{int} = 23.3 \text{ fb}^{-1}$. After a long shutdown, LHC was upgraded for Run II, to operate on $\sqrt{s} = 13$ TeV in 2015 and delivered 4.22 fb^{-1} of data by the end of 2015. In 2016 LHC continues operation on $\sqrt{s} = 13$ TeV and by the end of September the integrated luminosity already exceeded a value of 30 fb^{-1} [37].

The measurement of this dissertation is performed at the energy of 4 TeV per beam or at the center of mass energy $\sqrt{s} = 8$ TeV with 19.6 fb^{-1} of data. The same process was measured at $\sqrt{s} = 7$ TeV with about four times less amount of data by both CMS and ATLAS. These measurements are discussed in greater details in Ch. 2.5.

CERN's Accelerator Complex



LHC Large Hadron Collider SPS Super Proton Synchrotron PS Proton Synchrotron

AD Antiproton Decelerator CTF3 Clic Test Facility AWAKE Advanced WAKEfield Experiment ISOLDE Isotope Separator OnLine Dvice

LEIR Low Energy Ion Ring LINAC LINear ACcelerator n-ToF Neutrons Time Of Flight HiRadMat High-Radiation to Materials

© CERN2013

Figure 16: CERN's accelerator complex. Source of the figure: [34].

Table 2: Main parameters of LHC [31]

Circumference	27 km
Dipole operating temperature	1.9 K
Number of magnets	9593
Number of main dipoles	1232
Number of main quadrupoles	392
Number of RF cavities	8 per beam
Nominal energy, protons	7 TeV
Nominal energy, lead ions	2.76 TeV per nucleon
Peak magnetic dipole field	8.33 T
Min. distance between bunches	7 m
Design luminosity	$10^{34} \text{ cm}^{-2} \text{ s}^{-1}$
No. of bunches per proton beam	2808
No. of protons per bunch (at start)	1.1×10^{11}
No. of collisions per second	600 millions

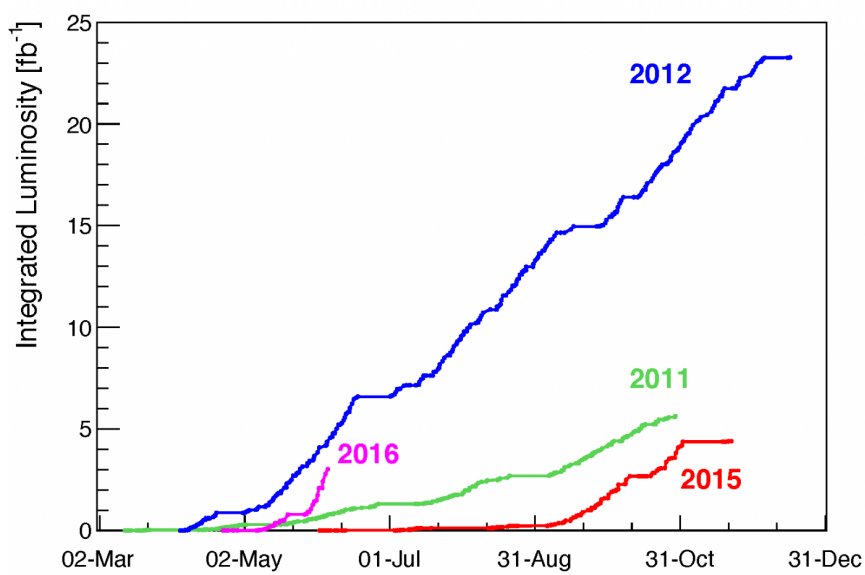


Figure 17: LHC integrated luminosity by year. Source of the figure: [35].

3.2 Compact Muon Solenoid

3.2.1 Introduction

The CMS is a general-purpose detector designed for detecting various highly energetic particles which are being produced in pp collisions at the LHC. The CMS has a broad program with goals of direct and indirect searches of the BSM physics including but not limited to supersymmetric particles. Its main feature is a huge magnet to create a magnetic field of 4T to curve charged particles in the tracking system and 2T outside to curve muons in the muon system.

The CMS detector is a cylindrically symmetric with a colliding beam as a central axis. Cartesian, cylindrical and spherical coordinates are all used to describe the CMS geometry, depending on the context. The x -axis of the CMS points towards the center of the LHC while the y -axis points vertically up. The direction of the z -axis corresponds to the counterclockwise direction of the LHC beam (Fig. 18, left). Cylindrical coordinates are defined as $r = \sqrt{x^2 + y^2}$, $\phi = \arctan(y/x)$. Instead of the polar angle θ , it is more convenient to use the pseudorapidity $\eta = -\ln \tan \theta/2$. A pseudorapidity changes from $\eta = -\infty$ to $\eta = +\infty$ for directions parallel to the beam axis with the value of $\eta = 0$ for a direction perpendicular to the beamlime. This variable is convenient for measurements because a distribution of a massless particle in η is nearly flat. The acceptance of the CMS in η is limited and varies from $|\eta| = 2.4$ to $|\eta| = 5.0$ depending on a subdetector.

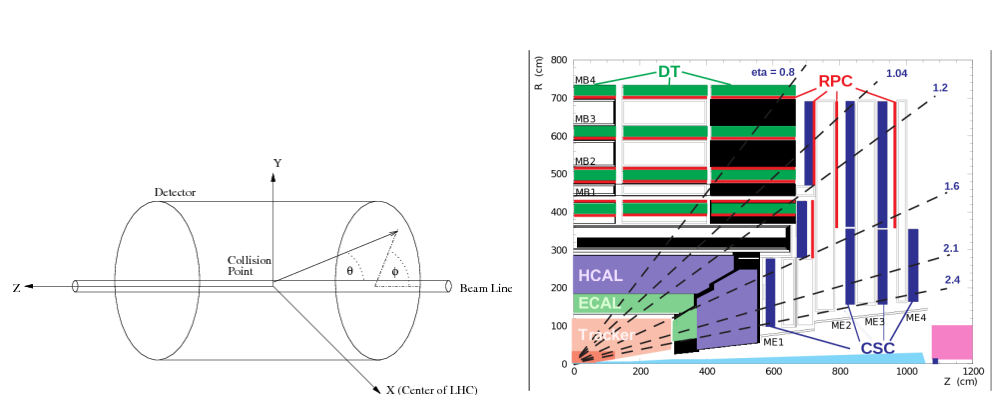


Figure 18: Left: CMS coordinate system. Right: pseudorapidity ranges for different CMS subdetectors.

The detector consists, from inner to outer layer, of a tracking system, an electromagnetic calorimeter (ECal), a hadronic calorimeter (HCal), a magnet and a muon system. Having the tracking system, ECal and HCal inside of a large solenoid makes the detector compact. A segment of a CMS slice in $r - \phi$ plane is shown in Fig. 19.

When a heavy particle is produced in a collision, it decays immediately, and we detect its long-living decay products including an electron, a photon, a muon, a neutral hadron or a charged hadron. Depending on the trace left by a particle in different subdetectors we can identify a particle. Electrons and positrons leave curved tracks in the tracking system and then induce showers in the electromagnetic calorimeter (ECal). Photons induce the same electromagnetic showers in ECal however, as neutral particles, they do not leave tracks in the tracking system. Hadrons normally travel through the ECal undisturbed and induce a hadronic shower in the hadronic calorimeter (HCal). Charged and neutral hadrons can be distinguished from each other by checking whether they leave a track in the tracking system or not. Muons are the only particles which penetrate through the ECal, the HCal and the magnet and leave tracks in the CMS muon system. Neutrinos are not detected by CMS.

843

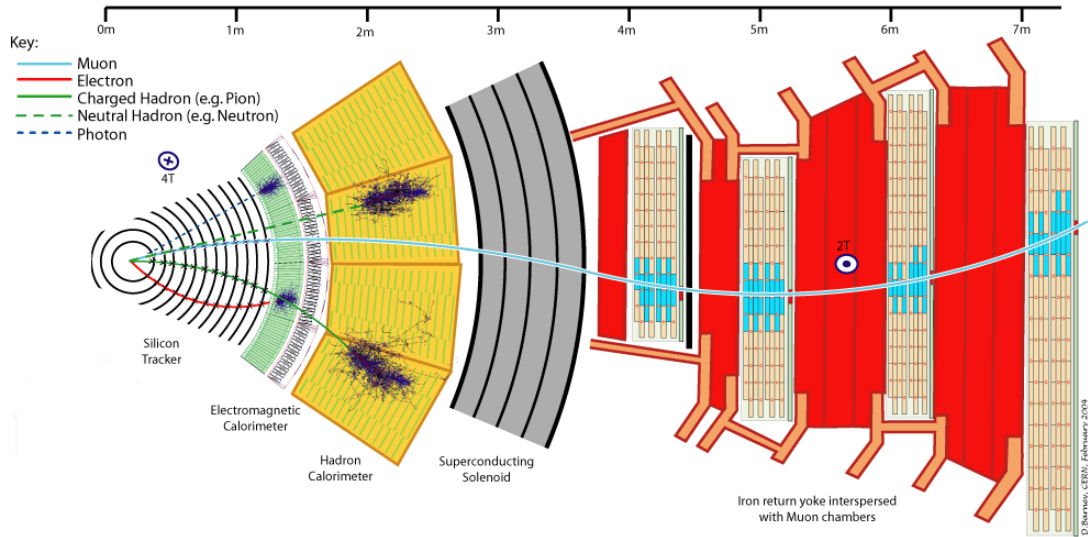


Figure 19: CMS slice.

844 All subdetectors are important for the $W\gamma$ measurement and the remainder of this chapter
 845 describes the subdetectors in greater details. Muons and electrons which we have as final state
 846 particles are both affected by CMS magnetic field allowing the tracking system and the muon
 847 system to measure their trajectory parameters and momenta. In this dissertation we use the
 848 information of the primary vertex determined by the tracking system to select our events. Also
 849 the tracker provide us the information about electrons trajectories and momenta in the electron
 850 channel and distinguishes between electrons and photons.
 851

852 3.2.2 Magnet

853 A magnetic field in a particle detector is necessary to measure momenta of charged particles
 854 by track curvatures. The higher the momentum is, the less a particles's path is affected by the
 855 magnetic field. In CMS it is done in the tracking system for all charged particles and in the
 856 muon system for muons.
 857

858 The CMS magnet is placed between layers of HCal and a muon system. It creates a magnetic
 859 field of 4T inside the magnet, for the tracking system, and 2T outside the magnet, for the muon
 860 system. It is necessary to have stronger field in the tracking system because a density of tracks
 861 is much higher there than in the muon system and also the tracking system is much smaller and,
 862 therefore, more significant curvature is necessary to measure the momentum with high precision.
 863

864 The magnet is made of superconducting wires. An electric current flowing in the wires creates
 865 a uniform field inside the solenoid and also provides a magnetic field of a certain configuration
 866 outside the solenoid.
 867

868 3.2.3 Tracking System

869 The tracking system measures track geometry including particles trajectories and locations of
 870 primary and secondary vertices and momenta of charged particles. It needs to disturb particles

as little as possible so that they can pass through. Therefore, just a few measurements must be enough to reconstruct the track. The accuracy of a measurement of each hit is $10 \mu\text{m}$.

The tracking system consists of silicon pixels and silicon strips (Fig. 20). Collision tracks start at the center and then cross the layers of the tracking system. Tracks are straight in $r - z$ plane and curved by the magnetic field in the $r - \phi$ plane. The acceptance of the tracker system in $r - z$ plane is geometrically limited by $\eta = 2.5$ ($\eta = -\ln[\tan \theta/2]$, where θ is a polar angle).

The pixel tracker is the closest subsystem of CMS to the collision point thus it experiences the largest particle flux: at 8 cm from the collision point the flux is about 10 million $1/(\text{cm}^2\text{s})$, and the pixel detector with its 65 millions sensors is capable to reconstruct all these tracks. It consists of three layers of cylinders in the barrel with radii of 4 cm, 7 cm and 11 cm and four disks in the endcap, two disks at each side. The tracker is designed in such a way that a single track hits multiple sensors. Then the trajectory is reconstructed based on how much charge is collected on each sensor. This allows us to reach a spacial resolution of 15-20 μm which is much smaller than a distance between sensors.

The strip tracker is placed right after the pixel tracker and occupies the detector volume up to 130 cm around the beam axis. The strip tracker consists of four parts: the tracker inner barrel (TIB), the tracker inner disks (TID), the tracker outer barrel (TOB) and the tracker endcap (TEC) as shown in Fig. 20. In the strip tracker there are over 15,000 sensitive modules with a total number of 10 million strips. Each sensitive module consists of a set of sensors, its support structure and readout elements.

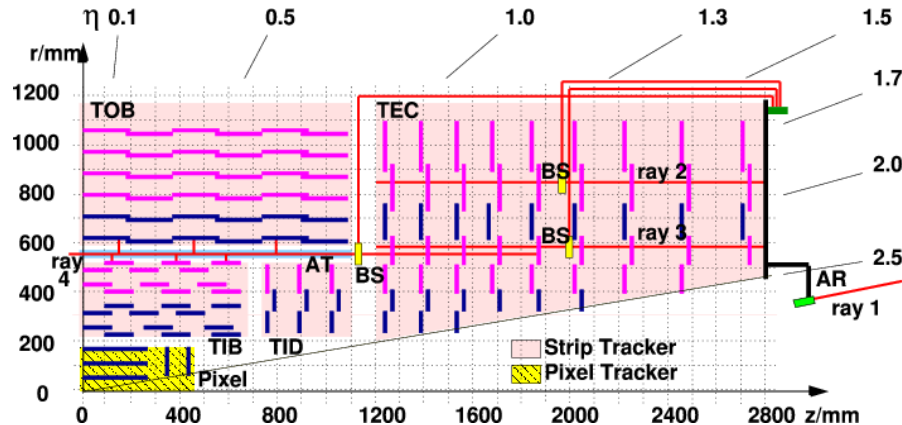


Figure 20: Slice of the CMS tracking system in $r - z$ plane.

3.2.4 Electromagnetic Calorimeter

The ECal measures energy of electrons and photons and also measures geometries of their trajectories. Electrons and photons interact with the ECal substance by inducing electromagnetic showers. Traces left by photons and electrons in the ECal are the same. To distinguish between these two particles, it is necessary to perform matching to the track in the tracking system. If there is a track, then there is an electron (or positron). If there is no track, then the particle is a photon.

The Ecal is a layer between the tracking system and the HCal. It is made of high-density lead tungstate crystals arranged in a barrel section and two endcap sections. The crystals work as scintillators. When electrons and photons pass through it, it produces light proportional to the

906 particle's energy. The scintillated light then is amplified by photomultipliers producing signals
907 on sensitive elements.

908 It is important for the ECal to be able to distinguish between high energetic photons and
909 pairs of lower energetic photons e.g. from a π^0 decay. It is especially difficult in the endcap
910 sections where angle between two photon trajectories is small. Ecal preshower located in front
911 of the endcaps which have much smaller granularity provide extra spacial precision. Their strips
912 are 2 mm wide compared to 3 cm wide crystals in the main volume of the ECal.
913

914

915 **3.2.5 Hadron Calorimeter**

916 The HCal is placed right after the ECal and is the last subdetector within the magnet. The
917 HCal measures energies of charged and neutral hadrons. In addition, the HCal determines the
918 track parameters. Match to the tracking system has to be done: if a matching track found, then
919 it is a charged hadron otherwise it is a neutral hadron.

920

921 The HCal consists of alternate layers of absorbers and scintillators. Hadrons hit brass or steel
922 plate of absorber producing secondary particles. When emerge into the scintillator, the particles
923 induce hadronic and electromagnetic showers and emit blue-violet light which is further shifted
924 to the green region and read out by special boxes within the HCal. The secondary hadrons pro-
925 duced during the interaction with the absorber interact with the next absorber producing more
926 showers in the next layers of scintillators and also affect the total energy deposit. All hadrons
927 must be stopped inside the layers of the HCal.

928

929 **3.2.6 Muon System**

930 Muons pass through the ECal, the HCal and the magnet without interacting. They are the only
931 particles which are registered in the muon system which is placed outside the magnet and which
932 is the largest part of CMS detector.

933

934 There are four concentric layers of muon detectors (stations) and iron return yoke between
935 them. Muons induce several hits in the muon stations which are later fitted and matched to the
936 tracking system measurements to provide the best possible resolution in the measurements of all
937 parameters of the muon's trajectory and momentum.

938

939 There are three types of muon chambers used in the CMS muon system: drift tubes (DTs),
940 cathode strip chambers (CSCs) and resistive plate chambers (RPCs). Overall, there are 1400
941 muon chambers including 250 DTs, 540 CSCs and 610 RPCs.

942

943 The system of DTs measures positions of muons in the barrel. Each DT chamber is about 2 m
944 by 2.5 m in size. It consists of 12 layers of aluminium which are grouped by four. There are up
945 to 60 drift tubes in a layer. The middle group of layers measures z -coordinate and two other
946 groups determine the perpendicular coordinate.

947

948 Each drift tube is 4 cm in width, is filled with a gas and has a wire inside. When a charged
949 particle passes through the volume, it ionizes atoms and the wire receives an electric charge.

950

951 CSCs are placed in endcap regions. CSCs are arrays of anode wires which are crossed by
952 copper cathode strips placed in a gas volume. When a charged particle penetrates to the gas
953 volume, it ionizes the gas. Electrons drift to the wires while ions move to the strips. Strips are
954 perpendicular to wires, thus, we measure two coordinates for each particle.

955

956 RPCs are parallel capacitors made of high-resistivity plastic plates with a space between
957 them filled with a gas. RPCs provide quick measurements of muon momenta and are used for

958 triggering.

959

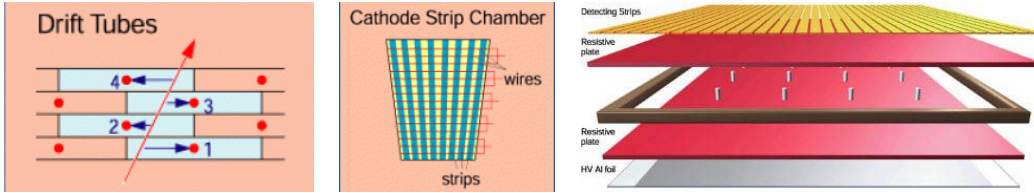


Figure 21: Components of the CMS muon system. Left to right: drift tubes, cathode strip chambers (CSCs), resistive plate chambers (RPCs).

960 3.2.7 Triggering and Data Aquisition

961 At peak luminosity, CMS experiences one billion proton-proton collisions per second which come
962 in bunches separated just by 25 ns from one other. New events come before the events from
963 the previous bunch crossing left the detector. To process the information from many different
964 collisions at the same time, data is stored in pipelines.

965

966 It is not technically possible to readout all these events. Moreover, we do not need most
967 of these events for a physics analysis because most of these events do not have a potential to
968 discover a new physics. We have resources to store about one hundred events out of one billion
969 that is why we need a trigger system which quickly decides what the best one hundred events are.

970

971 If the triggers were too loose, and we would select one hundred events too quickly, e.g., out
972 of a hundred million events, then CMS would not be able to process the rest 90% of events in a
973 givem set of one billion and we would lose 90% of potentially interesting events.

974

975 If the triggers were too strict, we would select, e.g, ten events out of one billion, not one
976 hundred and lose CMS potential to store and process data by 90% which would significantly
977 reduce our chances for a discovery.

978

979 Thus, the challenge of the trigger system is to select the best one hundred events out of one
980 billion and do that fast to be able to process every single event. To achive this goal, a two-level
981 trigger system was developed consisting from the Level 1 (L1) trigger and the high level trigger
982 (HLT) as shown in Fig. 22.

983

984 L1 is a hardware based trigger (Fig. 23). It uses information from the ECal, HCal and muon
985 system. L1 reduces frequency of coming events from 40 MHz to 100 kHz. Events which did not
986 pass the L1 trigger are lost forever while events which pass the L1 trigger are temporarily stored
987 to get checked by the HLT.

988

989 HLT is a software-based trigger. It uses information from all subdetectors and runs quick
990 reconstruction and identification algorithms to determine types of particles and their kinematics.
991 It reduces the number of events to 100 Hz. Events which did not pass HLT are lost forever.
992 Events which pass HLT are arranged into appropriate datasets depending on HLT selection cri-
993 teria they passed and stored for physics analyses.

994

995 3.2.8 Event Reconstruction

996 Where to place particle reconstruction, particle flow algorithm and MET? Check other theses

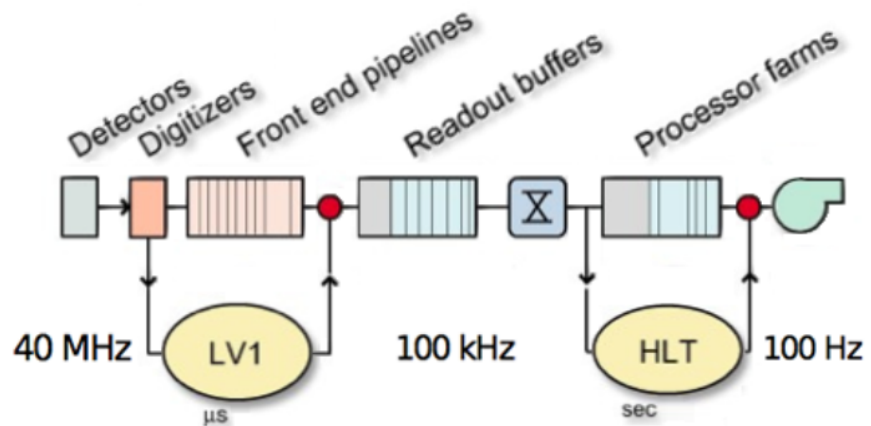


Figure 22: Two-level CMS trigger system.

997 Acceptance: particles which are too collinear and go to pipe; particles which get curved too
998 strongly

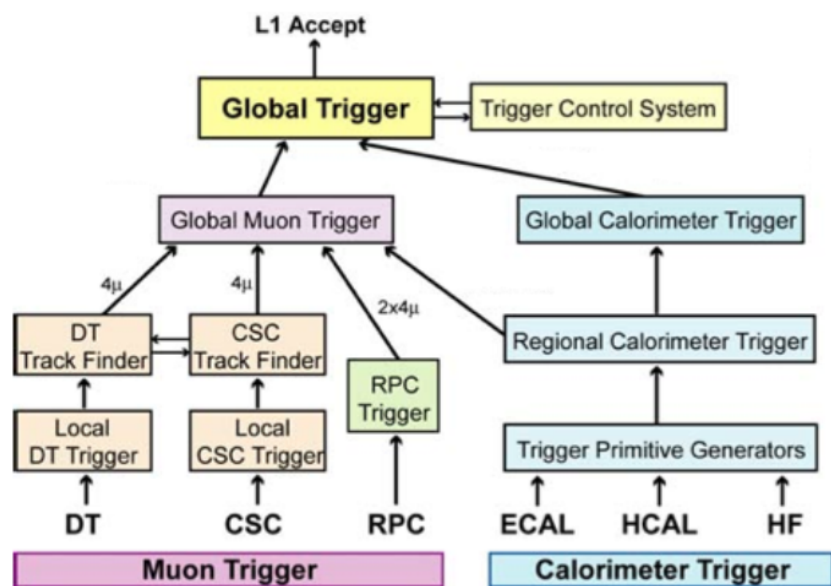


Figure 23: Level 1 CMS trigger system.

999 **4 CMS Tracker Alignment**

1000 4.1 Algorithm

1001 Why align?

1002 How to align?

1003 When align?

1004 How to check that your alignment is good?

1005

1006 A tracking system detects hits produced by a charged particle traveling through the detector.
 1007 In a presence of a constant magnetic field the particle has a helical trajectory. A reconstruction
 1008 algorithm determines the track parameters by fitting the positions of hits assuming the helix
 1009 trajectory.

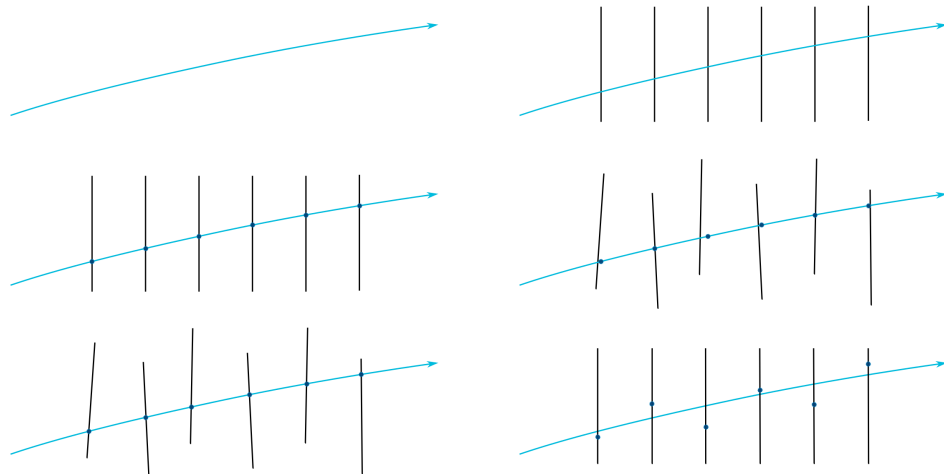
1010

1011 Better hit resolution and the location uncertainty lead to better precision of a measurement
 1012 of the track parameters. The location uncertainty depends on our knowledge of the positions and
 1013 orientations in space of the tracking system modules. The hit resolution in the CMS pixel detector
 1014 is $\sim 15 \mu\text{m}$. When the modules are mounted, their positions are known with precision of $\sim 200 \mu\text{m}$.
 1015 Thus, we need to know positions of modules 20 times better than they are known when mounted.

1016

1017 The procedure of the determination of the modules locations and orientations is called the
 1018 tracker alignment. The concept of the track-based alignment can be illustrated in the example of
 1019 the alignment of a toy tracker. When a charged particle passing through a detector (Fig. 24, top
 1020 left) it crosses a toy tracker which consists of six flat equidistant modules (Fig. 24, top right). If
 1021 the modules were placed exactly at their designed positions, we would observe the hits exactly at
 1022 the points where the track crosses modules at the points of ideal geometry (Fig. 24, middle left).
 1023 However, in a reality the positions and tilts of the modules are different from ones suggested by
 1024 the ideal geometry (Fig. 24, middle right). Hits, indeed, are recorded at the places where mod-
 1025 ules are actually mounted, not at the design ideal places (Fig. 24, bottom left). If we assumed a
 1026 tracker to be ideal and a track to be smooth, we would see that our hits are off-track (Fig. 24,
 1027 bottom right). So, we recalculate positions of the modules so that all the hits are laying on the
 1028 same smooth track (Fig. 25, top left). But these recalculated positions still do not coincide with
 1029 the actual positions (Fig. 25, top right). Then we record more and more tracks (Fig. 25, middle
 1030 left and right). We take into account them all and determine the alignment parameters with
 1031 necessary precision (Fig. 25, bottom left and right).

1032



1033 Figure 24: The alignment of a toy tracker, part 1.

When we record a track with a not-aligned tracker, we see that the track is not smooth. But

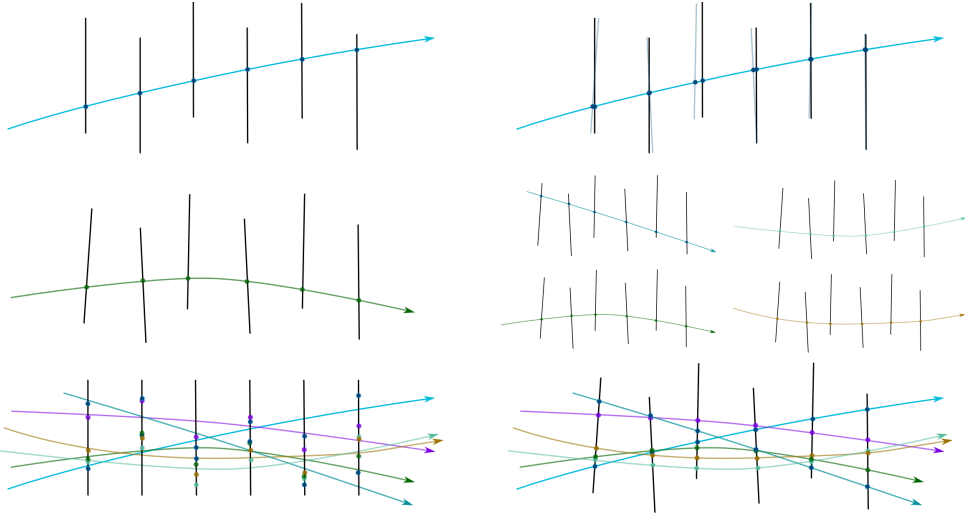


Figure 25: The alignment of a toy tracker, part 2.

that is because our knowledge of module positions is not exact. Thus, we can correct the positions assuming the track is smooth. But when we process the next track, we may find out that the positions have to be corrected again. Thus, we record many tracks and minimize residuals between measured and predicted hits.

The CMS tracker contains 1440 silicon pixel modules in PXB and PXF and 15148 silicon strip modules in TIB, TOB, TID, TEC.

The tracker alignment problem is the least squared problem. The expression to minimize is the following:

$$\chi^2(\mathbf{p}, \mathbf{q}) = \sum_j^{\text{tracks}} \sum_i^{\text{tracks}} \left(\frac{m_{ij} - f_{ij}(\mathbf{p}, \mathbf{q}_j)}{\sigma_{ij}} \right)^2 \quad (36)$$

where \mathbf{p} are parameters describing the tracker geometry, \mathbf{q}_j are parameters of the j^{th} track, $m_{ij} - f_{ij}$ are residuals, distances between the measured hit and a position predicted by the track fit, σ_{ij} is the Gaussian error of the measurement.

We can align the large substructures and individual modules with respect to their substructures. The parameters to align large substructures include their positions and orientations of the subdetectors (rotations). Thus, each subsystem is described by six parameters: three coordinates X, Y, Z and three angles α , β , γ . At the module level, we align positions and rotations with respect to the position s and angles of the corresponding large structure (Fig. 26). In addition, at the module level we align for surface deformations which are described by three parameters per sensor (Fig. 27).

A track can be described with five parameters.

We have two alignment algorithms: Millepede and HIP. Millepede performs a simultaneous fit of all alignment parameters and all track parameters while HIP perform iterative fits of alignment parameters \mathbf{p} and track parameters \mathbf{q}_j .

It is important to use different sorts of tracks for the alignment. Cosmic tracks pass through the detector vertically and do not allow us to connect different subdetectors to one another.

1064 Collision tracks originate from the collision point and go in all directions. However, those tracks
 1065 which cross TEC are all almost collinear and, therefore, it is difficult to measure z -coordinate of
 1066 TEC modules with collision tracks only.

1067

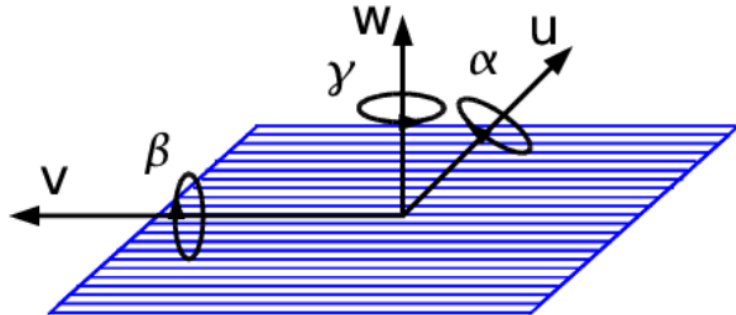


Figure 26: Alignment parameters.

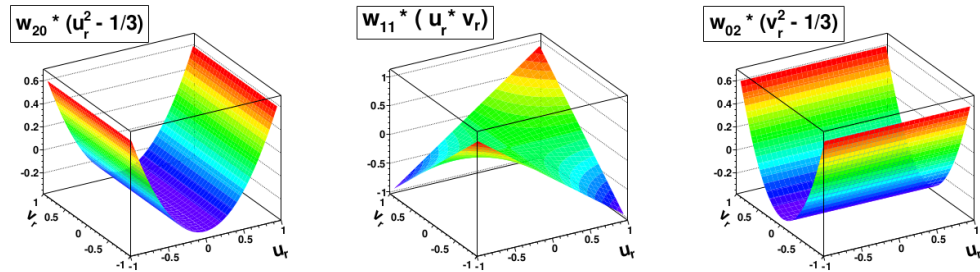


Figure 27: Surface deformations.



Figure 28: Track residuals.

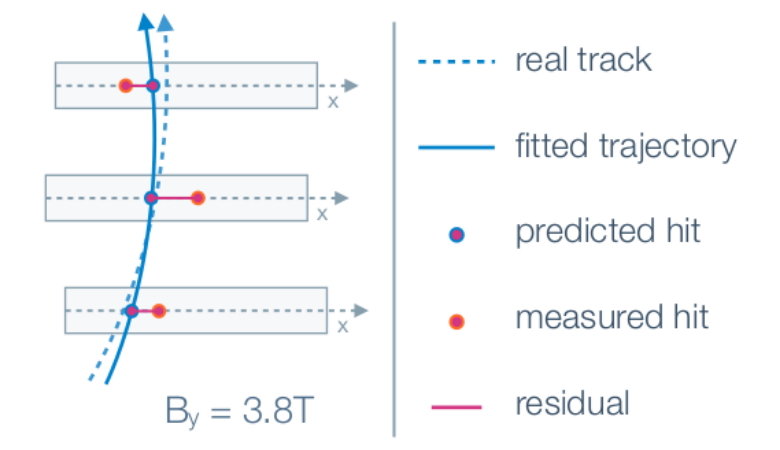


Figure 29: Track residuals.

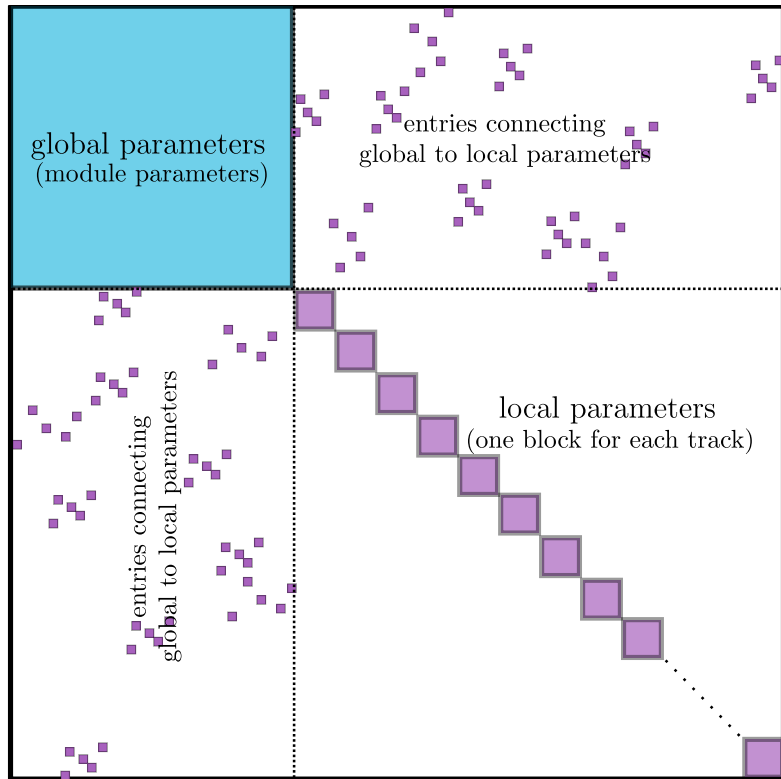


Figure 30: Track residuals.

1068 **4.2 Selected Results**

1069 CRUZET, CRAFT and first collisions of 2015

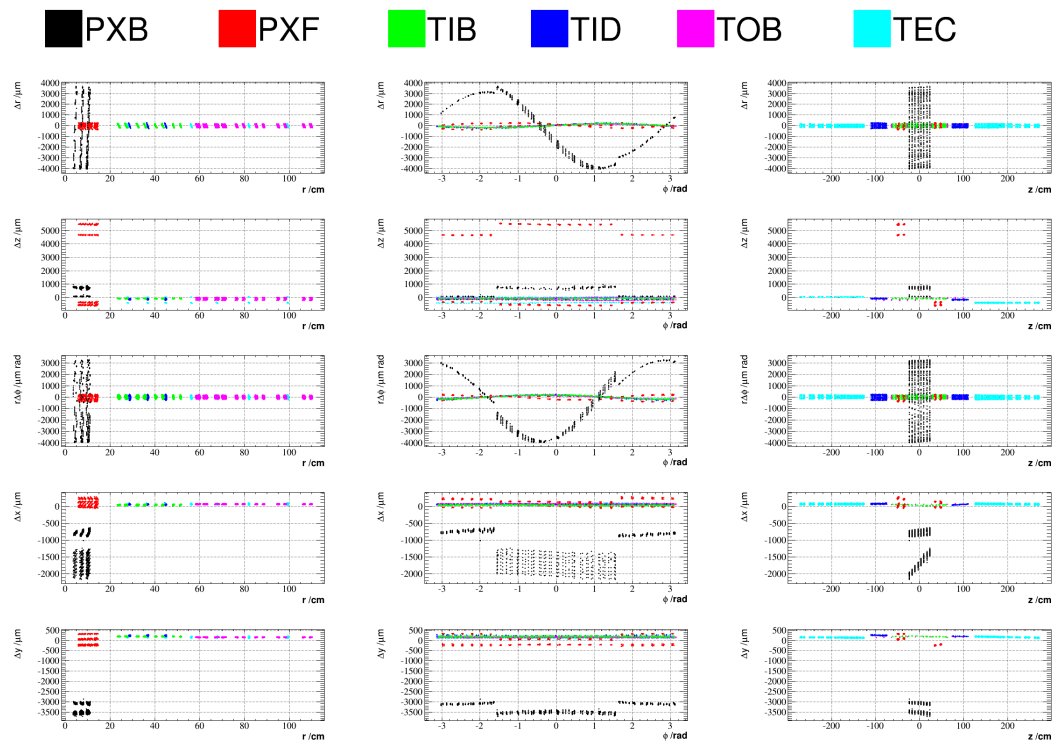


Figure 31: Geometry comparison plot of CRUZET 2015 object vs Run I.

1070 5 $W\gamma$ Cross Section Measurement

1071 Place analysis outline here

1072 References

- 1073 [1] Griffiths textbook
- 1074 [2] website: <http://www.isgtw.org/spotlight/go-particle-quest-first-cern-hackfest>
- 1075 [3] CMS Paper about Higgs boson discovery
- 1076 [4] ATLAS Paper about Higgs boson discovery
- 1077 [5] PDG
- 1078 [6] website: <https://science.nasa.gov/astrophysics/focus-areas/what-is-dark-energy>
- 1079 [7] Pich lectures: The Standard Model of Electroweak interactions
- 1080 [8] Halzen, Martin "Quarks and leptons"
- 1081 [9] <http://iopscience.iop.org/article/10.1088/0034-4885/70/1/R02>
- 1082 [10] Peskin, Schroeder
- 1083 [11] Lindsey's thesis (CMS Zg- ζ llg, 7 TeV)
- 1084 [12] website: https://www-d0.fnal.gov/results/publications_talks/thesis/snyder/html/node17.html
- 1085 [13] website: https://en.wikipedia.org/wiki/Cross_section_%28physics%29
- 1086 [14] LO (1969) theory paper
- 1087 [15] NNLO theory paper
- 1088 [16] NLO theory paper
- 1089 [17] aTGC paper
- 1090 [18] Senka's thesis (CMS Wg- ζ munug, 7 TeV)
- 1091 [19] D0 Combination of $W\gamma$, WW, WZ and VW using 8.6 fb-1 of 2 TeV $p\bar{p}$ collisions Phys.Lett.
1092 B718 (2012) 451-459
- 1093 [20] LEP Combination of WW and single W using 0.7 fb-1 per experiment of e^+e^- collisions at
1094 WW pair production energies arXiv:1302.3415
- 1095 [21] 7TeV Wg ATLAS paper
- 1096 [22] 7TeV Wg CMS paper
- 1097 [23] ATLAS WW using 20.3 fb-1 of 8 TeV pp collisions Submitted to JHEP
- 1098 [24] CMS WW using 4.9 fb-1 of 7 TeV pp collisions Eur. Phys. J. C 73 (2013) 2610
- 1099 [25] CMS WW using 19.4 fb-1 of 8 TeV pp collisions Submitted to EPJC
- 1100 [26] ATLAS VW ($V=W,Z \rightarrow jj$) using 4.6 fb-1 of 7 TeV pp collisions JHEP 01 (2015) 049
- 1101 [27] website: https://twiki.cern.ch/twiki/bin/view/CMSPublic/PhysicsResultsSMPaTGC#Figure_1_Limits_on_WW
- 1102 [28] CMS VW ($V=W,Z \rightarrow jj$) using 5.0 fb-1 of 7 TeV pp collisions Eur.Phys.J. C73 (2013) 2283
- 1103 [29] CMS 8 TeV WW lnlnmu
- 1104 [30] CMS 7 TeV Zg nunug
- 1105 [31] CERN brochure, <http://cds.cern.ch/record/1165534/files/CERN-Brochure-2009-003-Eng.pdf>

- 1107 [32] LHC TDR
- 1108 [33] website: <http://home.cern/topics/large-hadron-collider>
- 1109 [34] website: <http://cds.cern.ch/record/1621583/files/>
- 1110 [35] http://home.cern/sites/home.web.cern.ch/files/image/update-for_cern_people/2016/06/intlumirunall_image.png
- 1112 [36] website: <http://cds.cern.ch/journal/CERNBulletin/2014/24/News%20Articles/1706606>
- 1113 [37] website: <https://twiki.cern.ch/twiki/bin/view/CMSPublic/LumiPublicResults>